Ab initio determination of iron melting at terapascal pressures and Super-Earths core crystallization

Felipe González-Cataldo [*]

Department of Earth and Planetary Science, University of California, Berkeley, California 94720, USA

Burkhard Militzer

Department of Earth and Planetary Science, University of California, Berkeley, California 94720, USA
and Department of Astronomy, University of California, Berkeley, California, USA

We performed *ab initio* molecular dynamics simulations for pressures and temperatures from 300–5000 GPa and 3000–30 000 K in order to determine the equation of state of solid and liquid iron. By employing a thermodynamic integration technique, we derive the *ab initio* entropy and Gibbs free energy of both phases, which allows us to construct solid and liquid adiabats and discuss implications for shock experiments. We derive the melting line by equating solid and liquid Gibbs free energies and represent it by a Simon fit $6469\,\mathrm{K}(1 + (P/\mathrm{GPa} - 300)/434.82)^{0.54369}$. Near 300 GPa, our melting line is higher than extrapolations of previous melting laws that were obtained with simulations at lower pressures but is in very good agreement with the most recent experiments by Kraus *et al.* Science **375**, 202 (2022), that reached TPa pressures. The slope of our melting line is consistently steeper than that of our adiabats, which implies that the crystallization of iron in the cores of terrestrial planets always starts from their centers, like on Earth. We also construct models for Super-Earth interiors and compare with temperature profiles from published evolution models. These temperatures in many earlier publications are rather low, so that our melting line would imply completely frozen cores. Only later models by Stamenković *et al.* [Astrophys. J. **748**, 41 (2012)] and Boujibar *et al.* [J. Geophys. Res. Planets **125**, e2019JE006124 (2020)] consider a much wider range of interior temperatures, which imply that the core of Super-Earths may remain in a state with a partially molten core for a long time and the resulting buoyancy force will contribute to convection and the magnetic field generation.

DOI: 10.1103/PhysRevResearch.5.033194

I. INTRODUCTION

During the last two decades, several thousand exoplanets have been detected [1–3]. Measurements of their masses and radii have become more and more accurate, which allowed us to place constraints on their composition and better understand their atmospheres, formation, and evolution. Among the detected exoplanets, there are many Super-Earths, which are assumed to have a rocky composition but are larger than Earth. They are a particularly interesting type of exoplanets because they have no analogs in our solar system. Their interior structure has been the subject of numerous studies that have tried to constrain their composition [4–11]. Observations combined with modeling suggest that planets larger than 1.6 Earth radii are not purely rocky [12]. Recently, it has been proposed that Super-Earths may form from sub-Neptune sized planets that lose their H/He envelopes by irradiation from a supermassive black hole [13].

Developing realistic planetary interior models to infer the composition of Super-Earths requires knowledge of the equation of state (EOS) of the candidate minerals such as iron and silicates at extreme pressure-temperature conditions [14,15], which represents a challenge in planetary and materials science because the conditions of interest often lie outside the reach of laboratory experiments. Models predict that pressures in the interior of Super-Earth planets can exceed 1000 GPa at the core-mantle boundary, and temperatures can exceed 10 000 K [4,5,8]. More recently Boujibar *et al.* [16] studied the possible range of temperatures at the core-mantle boundary, for which a solid inner and a liquid outer core coexist, and showed that it depends on the planet's total mass and its core-mass fraction, but also sensitively depends on knowing the melting temperatures of iron at TPa pressures. The formation of a metallic iron core in these planets is driven by chemical differentiation and gravitational separation of liquid silicate-iron mixtures. The generation of magnetic fields is a direct consequence of the presence of liquid iron in the core. In the Earth, the crystallization of a solid inner core is assumed to be a major driver for the magnetic dynamo. Thus, studying the melting behavior of iron at pressures of Super-Earth interiors will contribute to a better understanding of their internal structure, core crystallization, and dynamo activity.

Because iron is the main constituent of the Earth's core, the characterization of its high-pressure properties have been

---

[*]f_gonzalez@berkeley.edu

of fundamental importance geophysics and condensed-matter physics. Planetary formation models predict it to be the main constituent of the core of the other terrestrial planets as well. The phase diagram of iron and, in particular, its melting line is not well understood for pressures exceeding 300 GPa, but both experiments and first-principles quantum mechanical simulations have shown that iron transforms from the body-centered-cubic (bcc) phase to the hexagonal-closed-packed (hcp) phase under pressure [17,18].

The melting curve of iron at pressures relevant to the Earth inner-core boundary (330 GPa) has been explored with different computational methods. Predictions published in the last two decades place the melting temperature of iron between 6300 K and 7300 K for this particular pressure [19–22]. Using thermodynamic integration, Alfè *et al.* [20] performed density functional theory molecular dynamics (DFT-MD) simulations and obtained a melting temperature of 6350 K, which was later confirmed by first-principles two-phase simulations in the microcanonical ensemble, using a relatively large number (1000) of atoms [21]. In a recent DFT study, Bouchet *et al.* [22] performed two-phase simulations in the canonical ensemble to extend the melting curve of bcc iron up to 1500 GPa. However, since the hcp structure is predicted to be the stable phase at these pressures [18,23–25], two-phase simulations of hcp iron may actually lead to higher melting temperatures. Nevertheless, the results in Ref. [22] are in good agreement with the aforementioned DFT studies [20,21].

A separate study by Sola and Alfè [26] showed that quantum Monte Carlo simulations, which treats correlation effects more accurately than DFT, tend to favor higher temperatures for ICB conditions, placing the melting temperature at 6900 ± 400 K for 330 GPa. Belonoshko *et al.* [19] fitted an embedded atom potential (EAM) to DFT simulations of hcp iron and performed two-phase simulations that predicted a melting temperature of 7100 K, similar to the quantum Monte Carlo predictions. In a recent paper, these authors coupled the EAM simulations to thermodynamic integration to obtain the free energies of bcc and hcp iron and obtained a melting temperature of 7190 K at 360 GPa for bcc and slightly lower, 6800 K, for hcp [27]. The most recent experiments on iron at TPa pressures by Kraus *et al.* [24] used dynamic shock and ramp compression [28,29] to show that at 330 GPa, iron melts from the hcp phase at 6230 ± 540 K, in agreement with previous experiments in diamond anvil cells by Anzellini *et al.* [30].

In this paper, we present a DFT-MD calculation of the melting curve of iron from 300 to 5000 GPa in order to cover the conditions present in Super-Earth interiors. The melting temperatures are obtained from free energy calculations that are based on a thermodynamic integration (TDI) method. With this technique, we determine which phase, liquid or solid, has lower Gibbs free energy for a given pressure and temperature. For a given pressure, the melting temperature is obtained by interpolating the free energy difference between solid and liquid phases as function of temperature. We also use the TDI method to derive the entropy as a function of temperature and pressure, which we enables to derive isentropes to characterize the temperature profiles in the cores of Super-Earths.

In Sec. II, we describe our computational methods and Gibbs free energy calculations. In Sec. III, we discuss our

melting curve and adiabats. We show that our melting temperatures are considerably higher than previous predictions that were extrapolated from data at lower pressure. We also predict that the melting curve is steeper than the adiabats, which implies that the crystallization of iron cores of Super-Earth would always start from the center, provided that core crystallization occurs in a planet's lifetime. In Sec. IV we build models for Super-Earth interiors focusing on planets with up to 1.6 Earth radii and 5.8 Earth masses. For relevant pressure conditions, we find that our melting temperature is much higher than the temperature profiles in available interior models, suggesting that the cores of Super-Earths are completely frozen over their entire lifetime.

II. COMPUTATIONAL METHODS

A. *Ab initio* techniques

Using density functional theory molecular dynamics (DFT-MD), we calculate the Gibbs free energy of iron for the solid and the liquid phases at specific pressure-temperature conditions. The melting temperature T_m is obtained when the Gibbs free energy difference

$$\Delta G = G_{\text{liquid}} - G_{\text{solid}}, \tag{1}$$

vanishes for a given pressure. For most solid calculations, we assume an hcp crystal structure, but we also performed a few calculations near 300 GPa using the bcc phase and one calculation for the melting temperature of the fcc phase at 5000 GPa.

An alternative approach for calculating the melting temperatures with computer simulations is the Z method, which has been applied to a number of other materials [31–37]. This technique is independent of the Gibbs free energy calculations, and is based on overheating the solid in the microcanonical (NVE) ensemble. The Z method relies on the fact that any solid system that has been sufficiently overheated will spontaneously melt, provided the simulations are long enough. As the latent heat is removed, the temperature of the system drops. If the amount of overheating is carefully calibrated, temperature will drop precisely to the melting temperature, T_m. Here we applied the Z method to study the melting of iron at different densities to compare with the melting points we derived from Gibbs free energy calculations.

We perform our DFT-MD simulations with the VASP code [38] using exchange-correlation functional of Perdew, Burke, and Ernzerhof [39]. We used a Mg-core pseudopotential of the projector-augmented wave type [40] with 14 valence electrons per atom (PAW-14) and a core radius of 1.16 Å. Some calculations were done using a Ne-core pseudopotential (PAW-16). Single-particle orbitals have been expanded in plane-waves with a cutoff of 1100 eV in all calculations. The DFT-MD simulations were carried out under the assumption of Born-Oppenheimer approximation. A time step of 0.5 fs was employed and the simulations lasted between 1.0 and 12 ps. We performed preliminary DFT-MD simulation in an hcp cell with 96 atoms using $2 \times 2 \times 2$ and Γ-only k-point grids. We found a that the energy and pressure were underestimated by 150 meV per atom and 14 GPa, respectively by the Γ-only k-point grid for pressures close to 5000 GPa.

All following simulations of both solids and liquids were then performed in a larger cell, containing 144 atoms (except for the bcc phase, where we employed a supercell with 128 atoms) with Γ-only k-point grid in order to converge the thermodynamic properties and prevent dynamic instabilities in the overheated solids. The same parameters were considered for the Z method calculations, with the exception of the simulation time, which was extended up to 8 ps in some cases to ensure the stability of the overheated solids. DFT-MD simulations with 144 atoms and a $2 \times 2 \times 2$ k-point grid showed that the total energy differs by less than 4 meV per atom respect to the Γ-only k-point grid. We also performed calculations with a larger cell of 180 atoms and obtained thermodynamic properties that were consistent with the 144 atom results, which we therefore considered sufficiently well converged for the purpose of this study. The c/a ratio in the hcp supercells was adjusted for every pressure-temperature condition in order to obtain hydrostatic conditions. For liquids, we used cubic cells with 144 atoms and Γ point to sample the Brillouin zone. In addition, DFT-MD simulations were performed with four other pseudopotentials available in VASP, which treat 8 or 16 electrons explicitly with PBE and PW91 functionals. These simulations also used 144 atoms and Γ-point sampling.

We also performed simulations in larger cells of up to 1296 atoms to test the convergence with respect to system size and simulation time. To do this, we trained an on-the-fly machine learning potential, as implemented in VASP 6. We trained the force field on a supercell of 144 iron atoms in the hcp phase using the PAW-16 pseudopotential at 12.938 g/cc and 6000 K. Simulations were carried out at both constant volume (NVT) and constant pressure (NPT), obtaining consistent results. After running them for over 25 ps, we observed no significant change in the pressure or free energy of the system with respect to our DFT-MD simulations performed with 144 atoms. We provide more details in the Appendixes.

B. Computation of Gibbs Free energies

Free energy calculations require the knowledge of the entropy, which is not directly accessible from the standard MD simulations. The anharmonic contributions to the free energy of iron are large [41], so a description of the solid phase with quasi-harmonic methods alone would not be appropriate and lead to incorrect melting temperatures. One of the available methods to address this problem is the thermodynamic integration (TDI), which is a general technique to determine the difference in Helmholtz free energy between two systems with potential-energy functions $U_a(\mathbf{r}_i)$ and $U_b(\mathbf{r}_i)$. By defining a hybrid potential $U_\lambda = U_a + \lambda(U_b - U_a)$, the difference in Helmholtz free energy between the two systems can be computed from

$$
\begin{aligned}
\Delta F_{a \to b} &= F_b - F_a \\
&= \int_0^1 d\lambda \left\langle \frac{dU}{d\lambda} \right\rangle_\lambda \\
&= \int_0^1 d\lambda \langle U_b(\mathbf{r}_i) - U_a(\mathbf{r}_i) \rangle_\lambda
\end{aligned}
\tag{2}
$$

where one averages over configurations $\mathbf{r}_i$ generated with forces derived from the hybrid potential.

In order to increase computational efficiency, we adopt a two-step TDI scheme as implemented in previous studies [42–48]. In this scheme, we introduce an intermediate system governed by a classical pair potential U_{cl}, which we constructed for every density and temperature by matching the forces along the DFT-MD trajectories [49]. For every temperature-volume condition, we perform a preliminary DFT-MD simulation and fit a new pair potential to the forces along the computed trajectory. More details on how this method is applied in liquid systems can be found in references [43,47], and Appendixes. The TDI procedure for solid systems is discussed in Refs. [42,45–47,50]. In the first integration step, one derives the free energy difference $\Delta F_{cl \to DFT}$ between the system interacting with the DFT potential U_{DFT} and the system governed by the classical pair potential U_{cl}. Because the classical forces match the DFT forces well, five equally spaced λ points are sufficient to obtain an accurate value of the integral in Eq. (2) in this step.

Then a second TDI step is performed in order to obtain $\Delta F_{ref \to cl}$, the free energy difference between the classical system and a reference system with known Helmholtz free energy F_{ref}. For liquids, we chose the ideal gas as the reference system. For solids, we employed an Einstein crystal as the reference system with a combination of two-body and one-body harmonic potentials for the classical system [42,45,47]. Recent work has shown that the correction by Frenkel *et al.* [51] to the free energy of a solid due to a fixed center of mass has been overestimated [52]. This correction overestimated of the stability of the solid phase, leading to melting temperatures that were slightly too high as was discussed for materials such as MgO and Be [50,52–54]. The alternate correction proposed in Ref. [52] is much smaller than the Frenkel correction and, in practice, it is equivalent to applying no correction because it is smaller than the error bars we obtain. Not applying the Frenkel correction due to a fixed center of mass increases the free energy of the solid, which slightly lowers the resulting melting temperature.

Since only classical Monte Carlo simulations are needed, the second integration step is computationally much less expensive (by factor of $\sim 10^{-5}$) than the first step that requires solving the Kohn-Sham equations. This remains true even though a larger number of simulations is required to accurately compute the integral in Eq. (2). The Helmholtz and Gibbs free energies of the DFT system are then obtained from

$$
F_{DFT} = F_{ref} + \Delta F_{ref \to cl} + \Delta F_{cl \to DFT}
\tag{3}
$$

and

$$
G_{DFT} = F_{DFT} + P_{DFT} V.
\tag{4}
$$

In order to align the Gibbs free energy of the solid and the liquid at the same pressure, we use the thermodynamic relationship

$$
G(P, T) = G_0 + \int_{P_0}^{P} V(P, T)\, dP,
\tag{5}
$$

where $G_0 = G(P_0, T)$, $P_0 = P_{DFT}$, P is the target pressure, and $V(T, P)$ is the respective volume of each system along an isotherm of temperature T that we obtain from a separate set of DFT-MD simulations.
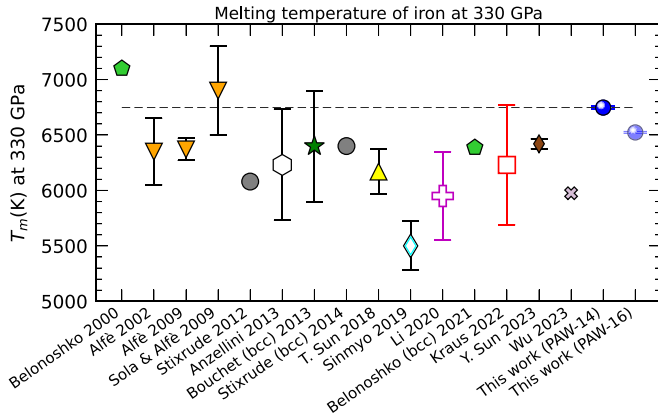
FIG. 1. Melting temperature of iron at 330 GPa, according to different studies. Open symbols denote experiments [23–25,30], while solid symbols represent predictions from *ab initio* simulations using different methods: TDI [20,26,27,55,57], two-phase simulations [19,21,22,58], free-energy based models [59], and the Lindemann law [18]. The temperatures from Refs. [27,57] have been interpolated from the values that the authors report at similar pressures.

For comparison purposes, we also implemented the Weeks-Chandler-Andersen (WCA) potential, given by

$$\Phi_{\text{WCA}}(r) = \begin{cases} 4\varepsilon\left[\left(\frac{\sigma}{r}\right)^{12} - \left(\frac{\sigma}{r}\right)^{6}\right] + \varepsilon, & r \leqslant 2^{1/6}\sigma \\ 0, & r > 2^{1/6}\sigma \end{cases} \quad (6)$$

because it was employed in one earlier study of iron [55]. We use it in lieu of our fitted pair potentials when we conduct test calculations for a few cases. This potential adopts the repulsive part of Lennard-Jones potential but removes its attractive part. Mirzaeinia *et al.* [56] computed the free energy of the WCA liquid by performing a TDI along a path at constant temperature to the low-density limit where the system's free energy is known analytically and corresponds to the ideal gas. This path provides an alternative to the integration path at constant density toward the limit of infinite temperature that we typically employ because our pair potential are finite at the origin. Still, we confirmed the accuracy of the subset of the results in Ref. [56] that are relevant for this study. Following Ref. [55], we set the potential parameters to each temperature an volume such that the reduced temperature $T^* \equiv k_B T/\varepsilon = 1.5$ and the reduced volume $\eta \equiv \pi\sigma^3/6V = 0.1$ to ensure that the system is in the liquid phase.

III. RESULTS

A. Melting at 330 GPa

Determining the precise melting temperature of iron at the Earth's inner-core boundary conditions, 330 GPa, is crucial for developing models of Earth's interior and understanding its core's crystallization and heat flow. Despite numerous attempts through simulations and experiments, a consensus on the precise melting temperature of pure iron at this pressure has been difficult to reach, as we illustrate in Fig. 1. This figure reveals discrepancies among the predictions for the melting temperature of iron at 330 GPa between different theoretical techniques, such as thermodynamic integration [20,26,27,55,57], two-phase simulations
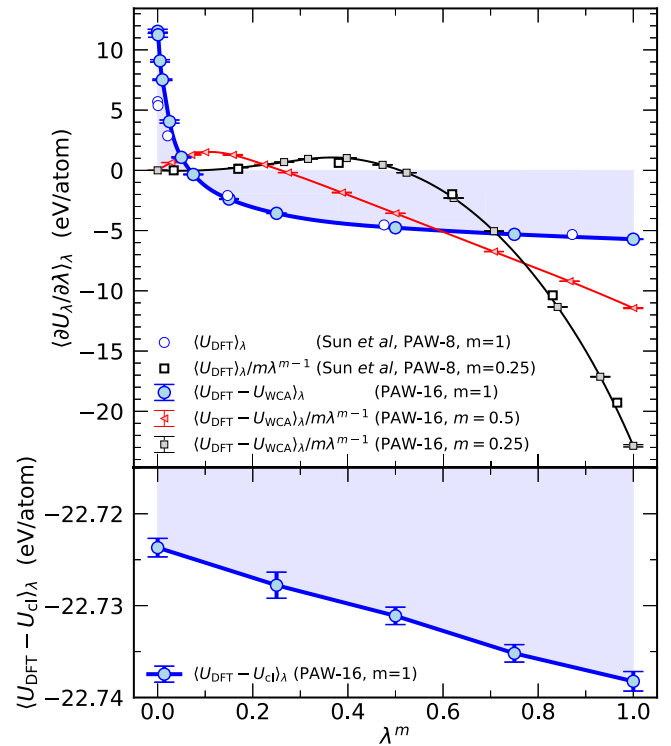

FIG. 2. Thermodynamic integration (TDI) of liquid iron at 330 GPa and 6400 K. The curves show the integrands of Eqs. (2) and (7). The integrand for our fitted pair potentials is a linear function of λ and varies by ~ 0.01 eV/atom (lower panel). Conversely, the different integrands for the WCA potential vary by several eV and some show considerable curvature (upper panel).

[21,22,58], free-energy based models [59], and the Lindemann law [18], as well as between experiments that have explored similar conditions [23–25,30]. Conducting experiments and accurate computer simulations has remained a challenge even at lower pressures of the core-mantle boundary [60], and the source of discrepancies among various study is often difficult to identify.

Because of these discrepancies, we have performed careful calculations with our TDI methods for solid and liquid iron at 330 GPa and temperatures ranging from 6000 K to 6800 K. As explained in Sec. II, we fit a new pair potential for every single thermodynamic condition so that our TDI calculations are independent from each other. For the solid, we use the Einstein crystal as the reference system with known free energy. The TDI is conducted in two steps. For the solid phase, we first integrate from the DFT system to a classical system with pair and harmonic Einstein forces. In the second integration step, we gradually turn off the pair forces.

For the liquid, we follow a similar procedure. First we switch from the DFT potential to a classical pair potential and then we turn off the classical forces, leading to a gas of noninteracting particles. To double-check our predictions, we repeated the TDI calculation for the liquid using the WCA potential instead of using our fitted pair potential as the intermediate system, as done in Ref. [55]. In Fig. 2, we show an example of the integrand in Eq. (2) as a function of λ for both TDI implementations for liquid iron at 330 GPa and 6400 K.

While for the pair potential the integrand is linear and varies by ~ 0.01 eV/atom (bottom panel), for the DFT $\rightarrow$ WCA integration the integrand has a large curvature in the same interval and varies ~ 18 eV/atom because the WCA potential does not represent the forces between the iron atoms very well.

The DFT $\rightarrow$ WCA integration can be performed directly as a function of λ if the integrand has been constrained by a sufficient number of points, each requiring computationally expensive DFT-MD simulations. However, fewer integration points may be used if a change of variables $\lambda \rightarrow \lambda^m$ is applied with $0 < m \leqslant 1$ in Eq. (2). This allows one to work with an integrand that varies more smoothly and obtain the integral

$$\Delta F_{\text{WCA}\rightarrow\text{DFT}} = \int_0^1 \frac{\langle U_{\text{DFT}} - U_{\text{WCA}} \rangle_\lambda}{m \, \lambda^{m-1}} d \, \lambda^m \qquad (7)$$

via Gaussian quadrature, as done by Sun *et al.* [55]. We sampled the integrand for this particular condition with 12 points, so we are not required to change the integration variable. We were able to obtain a smooth interpolation using cubic spline function for $m = 0.5$, $m = 0.25$ and the original integration ($m = 1$) as we show in Fig. 2. We obtained a consistent value of $\Delta F_{\text{WCA}\rightarrow\text{DFT}} = -3.893 \pm 0.007$ eV/atom that varies within the given error bars for all three values of m.

For 330 GPa, Sun *et al.* [55] reported a melting temperature of 6200 K, which is lower than our value of 6522 K. We primarily attribute this difference to a deviation in the computed Gibbs free energies of the liquid. In the two lower panels of Fig. 3, we show that our liquid Gibbs free energies for PAW-16 pseudopotential are about 35 meV/atom higher than the corresponding values by Sun *et al.*. While we could not extract sufficient details from Sun *et al.* article to fully explain this difference, we want to point out parts of the free energy calculations that we agree on and others that we do not. We added Fig. 2 for this comparison.

This figure also shows that using the WCA potential as classical system results in a very pronounced curvature of the integrand, which requires both a very careful sampling and a precise integration and interpolation methods to reduce the error in the final integral. Figure 2 shows that the integrand for the WCA potential varies by 18 eV/atom between $\lambda = 0$ to $\lambda = 1$, which makes it difficult to control the integration to meV/atom precision level. The lower panel shows when our pair potentials are employed, the integrand is approximately linear and varies by only 0.013 eV/atom. Furthermore, the WCA integral is very sensitive to the quality of the individual points because one needs to capture the curvature of the function correctly. For example, removing 3 out of 12 points can introduce differences of more than 100 meV/atom in the resulting integral.

We agree with Ref. [55] on the average energy of the WCA potential [56]. Our value of $\langle U_{\text{WCA}} \rangle_{\lambda=0} = 33.1 \pm 0.6$ meV/atom agrees with the 33.9 ± 0.3 meV/atom found by Sun *et al.* at their smallest value of $\lambda = 10^{-6}$. They implemented the TDI between the DFT and WCA potentials in a slightly different way, $U_\lambda = U_{\text{WCA}} + \lambda U_{\text{DFT}}$, which requires to integrate $\langle U_{\text{DFT}} \rangle_\lambda$ (open circles and open squares in Fig. 2) instead of our expression, $\langle U_{\text{DFT}} - U_{\text{WCA}} \rangle_\lambda$ (filled symbols).
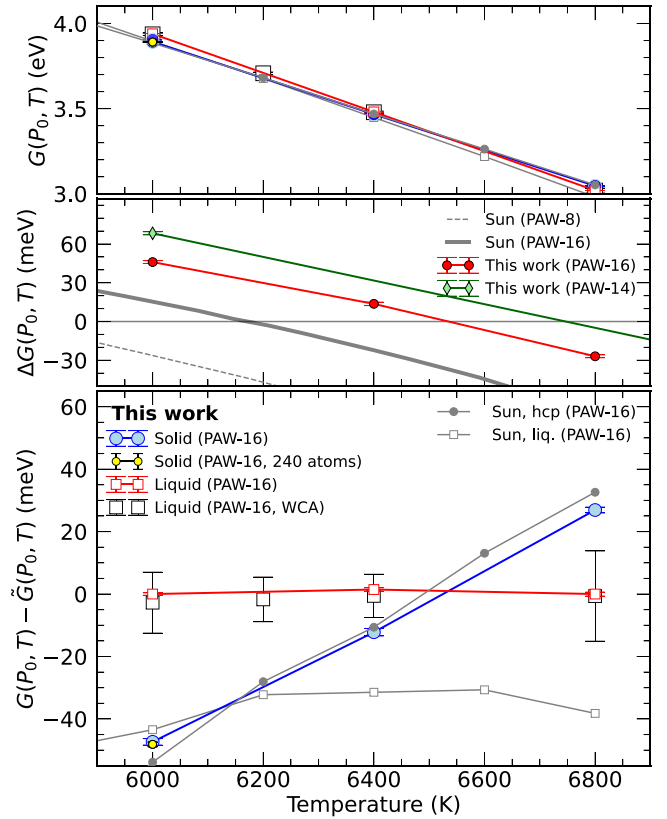

FIG. 3. Gibbs free energies per atom of solid (hcp) and liquid iron at $P_0 = 330$ GPa obtained from TDI using the PAW-16 pseudopotential. Top: original energies of each phase. Middle: Gibbs free energy difference $\Delta G = G_{\text{liq}} - G_{\text{sol}}$. Bottom: We plot the liquid and solid Gibbs free energies with respect to $\tilde{G}(P_0, T) \equiv \tilde{G}_0 - S_0 (T - T_0)$ (with $S_0 = 13.35 \, k_B$, $T_0 = 6000$ K, and $\tilde{G}_0 = 3.939$ eV), which is an linear approximation for $G_{\text{liq}}(P_0, T)$. TDI calculations of G_{liq} using our fitted pair potential (open red squares) and the WCA potential (open black squares) give consistent values, but the latter approach yields much larger error bars. We compare our results to those from Sun *et al.* [55].

Sun *et al.* performed the their TDI calculations using the PAW-8 pseudopotential, which means their values of $\langle U_{\text{DFT}} \rangle_\lambda$ differs from ours even in the limit of $\lambda = 0$, as we can see in the Fig. 2. Sun *et al.* then corrected their resulting Helmholtz free energies F_1 to achieve PAW-16 precision F_2 using free energy perturbation theory,

$$e^{-\beta(F_2 - F_1)} = \langle e^{-\beta(E_2 - E_1)} \rangle_1, \qquad (8)$$

which does not correct the pressure. Before this correction, Sun *et al.* reported $\Delta F_{\text{WCA}\rightarrow\text{PAW}-8}^{\text{Sun}} = -3.823$ eV/atom with PAW-8 pseudopotential (Fig. 4 in Ref. [55]), which is 70 meV/atom higher than we obtained with the PAW-16 pseudopotential. Sun *et al.* reported a smaller value of 53 meV/atom for the Helmholtz free energy difference between PAW-8 and PAW-16 pseudopotentials.

On the other hand, as we can see in the bottom panel of Fig. 2, our implementation of TDI, which involves fitting a pair potential that matches the interatomic forces at this specific temperature and pressure, is much less sensitive to the sample quality and interpolation methods because

$\langle U_{\mathrm{DFT}} - U_{\mathrm{cl}} \rangle_\lambda$ changes by much less and varies mostly linearly with λ. The choice between using a linear, Gaussian quadrature, or spline interpolation method, and whether we perform the integral directly or using the change of variables in Eq. (7), varies the integral by less than 10^{-4} eV/atom ($\Delta F_{\mathrm{cl} \rightarrow \mathrm{DFT}} = -22.7313 \pm 0.0005$ eV/atom). Even if we use two points only, $\lambda = 0$ and $\lambda = 1$, we can obtain the same value of the integral within 0.3 meV/atom. Therefore, our implementation of TDI is more robust than an integration that uses the WCA potential.

In Fig. 3, we show the resulting Gibbs free energy of liquid and solid iron at 330 GPa that we obtained from TDI results in Fig. 2, using both the WCA and our fitted pair potentials. We repeated these calculations for 6000, 6200, and 6800 K and compare the results between the two TDI implementations for liquids. Our Gibbs free energies of solid iron are in very good agreement with those provided by Sun *et al.* [55], and a calculation we have done with a larger simulations cell with 240 atoms confirms the convergence with respect to the system size. As we can see in the bottom panel, there is remarkable agreement between our two implementations of TDI for liquids. But when we utilize our fitted pair potential, the error bars on the Gibbs free energy are an order of magnitude smaller than for the WCA potential.

However, we observe a systematic offset of $\sim$35 meV/atom between our calculated Gibbs free energies for liquid iron and those reported by Sun *et al* [55]. Their results rest on a single TDI calculations with the WCA potential for a temperature of $T_0 = 6400$ K. Values for all other temperatures are calculated along the isobar by utilizing the thermodynamic relationship, $G/T = G_0/T_0 - \int_{T_0}^T H/T^2 \, dT$. So if there is an offset at 6400 K, all other Gibbs free energy values will be shifted, while our calculations for different P-T conditions are independent.

The middle panel of Fig. 3 shows that our solid and liquid free energies become equal at a temperature of 6523 ± 8 K, which is our prediction for the melting temperature at 330 GPa using the PAW-16 pseudopotential. In the same panel we show that when we repeat the calculation with the PAW-14 pseudopotential, $\Delta G = G_{\mathrm{liq}} - G_{\mathrm{sol}}$ increases by a modest amount of 20 meV/atom, which implies a melting temperature increase of approximately 200 K. In Ref. [55], the authors derived a ΔG value of 32 meV from perturbation calculations, which very close to the our result that we with full TDI calculations. The deviation between the two ΔG values is within the error bars of most numerical methods (see Fig. 1).

Using the PAW-14 pseudopotential, we find a melting temperature of 6747 ± 14 K at 330 GPa. Previous free energy calculations of hcp iron performed by Alfè *et al.* [20,61] used a nonstandard PAW-8 pseudopotential that mimicked the inner electrons by introducing a repulsive interaction via a classical pair potential correction in the PW91 functional. Their results point towards a lower melting temperature of $\sim$6350 $\pm$ 300 K, with an additional error of 300 K associated to the inherent DFT inaccuracies, including the choice of different pseudopotentials. This is close, but still lower, to our prediction using the PAW-16 pseudopotential. A later work by Sola and Alfè [26] revisited these calculations using diffusion Monte Carlo calculation that incorporate correlation effects

more accurately, and obtained a higher temperature of 6900 K $\pm$ 400 K for 330 GPa.

We have found, in agreement with other authors [20,55,57,61] that the predicted melting temperature of iron depends on the pseudopotential used, and the discrepancies become particularly pronounced when the 3p electrons are not considered. In order to address this issue in more depth, we performed a detailed study on how much the Gibbs free energies of liquid and solid iron are affected by the choice of the pseudopotential. For four additional VASP pseudopotentials, we redetermined the pressure-density relation along an isotherm, recomputed the free energies and melting temperatures. We performed these calculations for the three pressures of 300, 3000, and 5000 GPa to cover the entire pressure range of interest. We considered two PBE and two PW91 pseudopotentials with 8 and 16 valence electrons per atom, respectively. In the case of the eight-electron pseudopotentials, the 3s and 3p electrons are frozen while they were treated explicitly for the 16-electrons per atom pseudopotentials. We always find consistent melting temperatures when we switched between PBE and PW91 functionals for calculations with pseudopotentials that have the same number of electrons. Furthermore, the predictions with the small-core pseudopotentials, that treat 16 electrons per atom explicitly, were consistent with those from the 14 electrons per atom pseudopotential that we employed for most calculations in this paper, and the difference in the resulting melting temperatures are small, about $\sim$200 K, as we show in Fig. 3.

However, when we switched to the eight-electron PBE and PW91 pseudopotentials, the Gibbs free energies of solid and liquid iron were not affected equally. For these pseudopotentials, the liquid-solid Gibbs free energy difference at 300 GPa was $\sim$50 meV per atom lower than we had obtained with the 14-electron pseudopotentials. This reduced our predicted melting temperature at 300 GPa by 600 K to approximately 6200 K, which is in good agreement with the PAW-8 calculations by Sun *et al.* [55] who also used an 8-atom pseudopotential. Shock experiments from Yoo *et al.* [62] also suggest, as we do, a higher melting temperature. However, at 300 GPa, they report a melting temperature of 6720 K, which is 250 K above our predicted melting temperature using PAW-14 and 470 K below using PAW-16 at this pressure. These results by Yoo *et al.* [62] were recently reinterpreted by Kraus *et al.* [24], suggesting a much lower melting temperature at shock conditions that is consistent with their measurements and previous experiments by Anzellini *et al.* [30]. Despite of these differences, we find very good agreement among the predictions from various pseudopotentials for the volume and entropy differences upon melting.

B. Thermodynamic stability of the bcc phase

Other studies have considered that iron melts from the bcc phase at these conditions [27,57,58,63] because it has been argued that this phase may become stable at Earth inner-core pressures via a self-diffusion mechanism [64–66]. However, the bcc phase has not been observed in experiments at these conditions [23–25,67] and the size-dependent anomalies of the bcc cell are still controversial [68]. In Ref. [27],

Belonoshko *et al.* used thermodynamic integration to compute the free energy differences between the hcp, bcc, and liquid phases of iron at 120 and 360 GPa. While the simulations were done with classical molecular dynamics using the EAM, which does not take the electronic entropy into account explicitly, the contribution from the electrons to the free energy was obtained from *ab initio* calculations to correct the EAM-based free energies. Their results show that the free energy of the bcc structure is lower than that of hcp by $\Delta G = G_{hcp} - G_{bcc} = 23$ meV/atom at 360 GPa and 6000 K and that the resulting melting temperature of iron in the bcc phase is 7190 K at 360 GPa, higher than the melting temperature of hcp at the same pressure (6800 K). However, our TDI calculations based on DFT-MD at these conditions indicate that the free energy of the bcc structure is considerably higher, hence less stable than hcp, with $\Delta G = G_{hcp} - G_{bcc} = -65$ meV/atom and a melting temperature for hcp of 6922 K at 360 GPa. At 330 GPa, this difference is -57 meV, favoring hcp at Earth inner-core boundary pressures. Therefore, although our calculations show that the hcp is much more stable than the bcc structure, our resulting melting temperatures for both structures are still similar.

In Ref. [57], Y. Sun *et al.* implemented a different type of thermodynamic integration but used a similar approach to that of Ref. [55], where they performed the TDI calculations with PAW-8 and corrected the free energies to PAW-16 accuracy through free energy perturbation. In contrast to the findings of Ref. [27], and along with our predictions, the authors obtain a higher melting temperature for the hcp phase than for the bcc phase at 360 GPa: 6692 ± 45 K and 6519 ± 80 K, respectively. Near 330 GPa, the authors report melting temperatures of 6357 ± 45 K and 6168 ± 80 K for hcp and bcc, respectively. This study, like ours, also suggest that hcp should be the stable phase of pure iron at core conditions, as this phase has lower free energy and higher melting point than bcc, in agreement with our results. However, the authors of Ref. [57] suggest that PAW-8 underestimates the melting temperatures by more than 600 K compared to PAW-16, while in Ref. [55] the authors suggest that this difference is 400 K. Going beyond free energy perturbation, our TDI calculations using PAW-16 suggest that this difference is actually 466 K, as we obtain a melting temperature of 6060 ± 8 K with PAW-8. This is ~ 200 K higher than the melting temperatures reported in Refs. [55] and [57] with the same pseudopotential. Again, the melting temperatures reported in Ref. [57] using PAW-16 are ~ 200 K lower than our prediction with this pseudopotential.

C. Melting at TPa pressures

Pressures in the cores of Super-Earths can easily reach several TPa [5,8,12,69]. Extending the melting curve of iron to such conditions is thus important to determine whether such planets have solid or liquid cores. In Fig. 4 we show the Gibbs free energy difference ΔG between solid and liquid iron at different pressures as a function of temperature. Negative values of ΔG indicate that the liquid phase is more stable than the solid, while $\Delta G = 0$ corresponds to the melting temperature at the given pressure. Since we have determined that the hcp structure has a lower Gibbs free energy at Earth's core conditions, and based on stability arguments of iron phases in
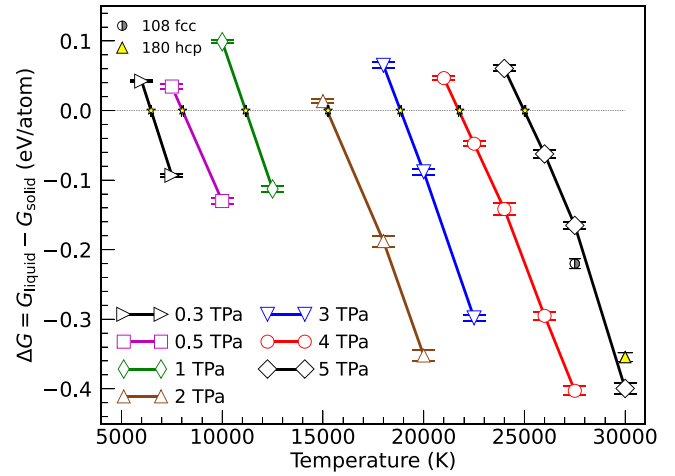

FIG. 4. Gibbs free energy difference between solid and liquid iron at different pressures obtained with the PAW-14 pseudopotential using 144 (except for 108 fcc and 180 hcp). No correction due to a fixed center of mass (Frenkel correction) has been applied to the free energy of the solid. Negative values of ΔG favor melting. Half-filled circle: fcc iron (108 atoms). Yellow-filled triangle: hcp iron (180 atoms). Yellow stars denote the melting temperature at each pressure.

Ref. [18], we adopted the hcp structure to perform all other calculations at higher pressures in this paper. Figure 4 shows that ΔG is a sufficiently linear function of temperature. We therefore use a linear interpolation for $\Delta G(T)$ to determine the temperature at which $\Delta G = 0$ for every pressure. The resulting melting points are shown in Fig. 5 along with the isochores we derived using the Z method. Previous *ab initio* studies of the melting curve of iron are also shown for comparison.

First, we notice that the melting temperatures we predict using the Z method are slightly higher, $T_1 = 11850$ K and $T_2 = 25030$ K at $P_1 = 1008$ GPa and $P_2 = 4518$ GPa, respectively, which agree with our melting curve within an 8% relative error. This also means that iron can withstand significant overheating without melting, as reported in recent shock experiments [70], with critical superheating temperatures 10% to 16% higher than the melting temperatures, but not as high as the critical limit of 23.1% [31]. Although the Z method can provide a close upper limit for the melting temperature, it is susceptible to waiting times required for the sample to melt [32], especially in the vicinity of the melting temperature. In addition, it is not clear what the appropriate electronic smearing should be in the microcanonical ensemble simulations of the Z method, which is particularly important for metals like iron, as the evolution of temperature and pressure of the system depends on this choice. In practice, this means that the ions are not in equilibrium with the electrons, as they follow a Fermi distribution with an associated temperature that is different to that of the ions. If we correct for this effect by considering a smearing of $\sigma = k_B T_{eq}$, where T_{eq} is the equilibrium temperature that the ions reached in the original Z method calculations, we obtain a melting temperature of 10 500 K at 969 GPa for the density of 17.44 g cm^{-3}, which is in much better agreement with our melting curve that we derived from free energies. Nevertheless, we obtained the specific heat of
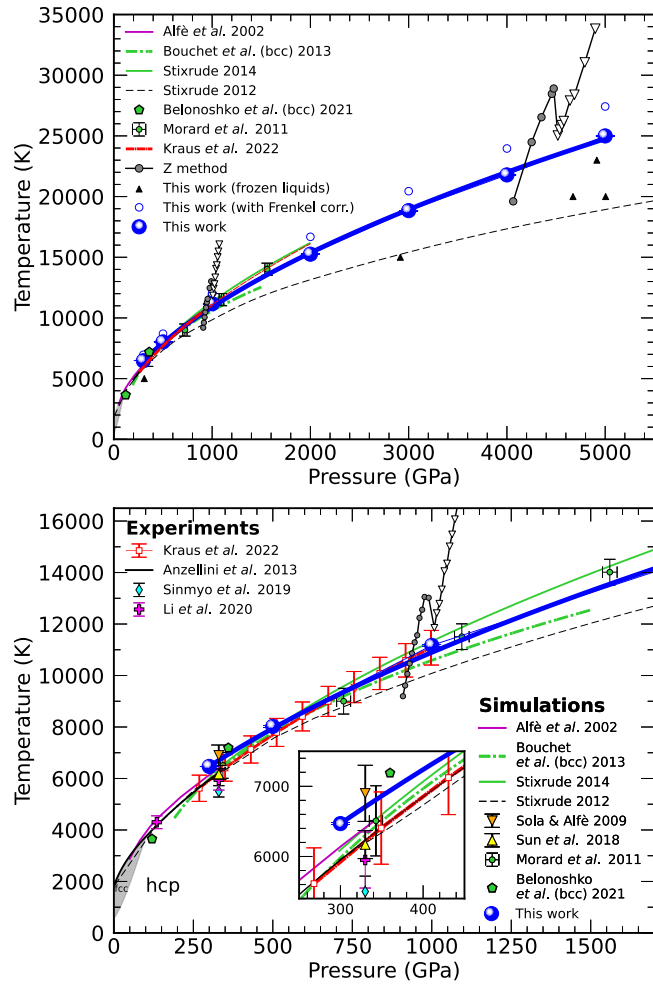
FIG. 5. Melting curve of iron from this study compared with previous *ab initio* simulations [18,20,22,26,27,55,58,63] and experiments [23–25,30]. Isochores of densities 17.44 and 27.23 g cm^{-3} obtained using the Z method are shown in black filled circles (solid) and open triangles (liquid). Liquids frozen during the simulation are shown in black filled up triangles. Open blue circles correspond to the melting points using the Frenkel correction, which overestimates the melting temperatures.

liquid iron from the slope of the Z curve in energy-temperature space, which yields $C_V^{liq} = 5.11 \, k_B$/atom along the 17.44 g cm^{-3} isochore that spans through pressures near 1000 GPa, as we see in Fig. 5. This value agrees with the recent experiments by Kraus *et al.* [24], who estimated a value of $4.2 \pm 1.0 \, k_B$ at similar conditions. At a density of 27.23 g cm^{-3}, the solid and the liquid have a comparable specific heat of $C_V^{sol} = 4.94 \, k_B$ and $C_V^{liq} = 5.64 \, k_B$, respectively. The Z method approach is independent from our TDI method and confirms our melting predictions over a wide pressure interval.

Second, we find that our melting temperatures are higher than the estimations from vibrational frequencies using the Lindemann melting criterion [18]. The difference is as large as 5000 K (20%) at 5000 GPa, which shows that iron can withstand significant thermal vibration at high pressure before undergoing melting. At 1500 GPa, our melting line is approximately 750 K higher than the bcc iron melting line of Bouchet

et al. [22] who used the two-phase (TP) method to calculate the melting curve up to this pressure. From heat-until-it-melts simulations, the authors conclude that the melting temperature does not significantly depend on whether hcp or bcc crystal structure is used at the pressures of interest and decided to use the bcc structure in all their TP simulations. They acknowledged, however, that calculations with a metastable phase could lead to an underestimation of the melting temperature. While the stability of the bcc structure at Earth's ICB conditions is still a matter of debate [64,66,71,72], the hcp structure has been predicted to be the most stable structure for a wide range of pressures and temperatures [18].

Furthermore, for temperatures as high as 20 000 K, we observed that some of our simulation of liquid iron froze spontaneously within a few picoseconds at pressures between 2500 and 5000 GPa. This has also been confirmed by the recent experiments of Kraus *et al.* [24] that report fast crystallization in the nanosecond time scale. The filled triangles in Fig. 5 mark these conditions. Many of them are at substantially higher temperatures than the extrapolated melting law by Bouchet *et al.*, which underlines that the melting temperature of iron at TPa pressure must be considerably higher than this extrapolation predicts.

At 5 TPa, the Gibbs free energy between the hcp crystal and liquid iron is less than 60 meV/atom at 24 000 K and 26 000 K, which indicates this temperature is close to the melting line (see Fig. 4). A study of the free energy of iron obtained from phonon calculations in the quasi-harmonic approximation (QHA) [18] predicted an hcp-to-fcc transition at 5.8 TPa, with a steep Clapeyron slope at higher temperatures, implying that the transition should occur at lower pressures for higher temperatures and that both phases should have the same Gibbs free energies at the phase boundary. Therefore, we decided to perform one additional calculation of the Gibbs free energy of iron in the fcc phase at 5 TPa for 27 500 K in order to determine whether the fcc phase has a significantly lower Gibbs free energy than the hcp structure, which would have an affect on the predicted melting line. We derived a Gibbs free energy difference of $G_{fcc} - G_{hcp} = 56$ meV per atom, which means that even at this high temperature the hcp phase is still more stable than the fcc phase, even though predictions from Ref. [18] using QHA indicate that the transition to the fcc phase at 5 TPa should occur at 13 300 K. Therefore, we conclude that anharmonic contributions to the free energy play an important role, which is consistent with the underestimated melting temperatures inferred using the Lindemann criterion in Fig. 5 based on QHA.

We also studied finite-size effects at this pressure by performing one calculation at $T = 30\,000$ K in a larger hcp cell with 180 atoms. The difference in Gibbs free energy between the 144 and 180 atoms cells was found to be 45 meV, which is shown by the yellow triangle in Fig. 4. This means that the effect of size on the melting temperature is negligible, as our 144 atoms cell is large enough.

We fitted our melting temperatures from 300–5000 GPa to a Simon equation,

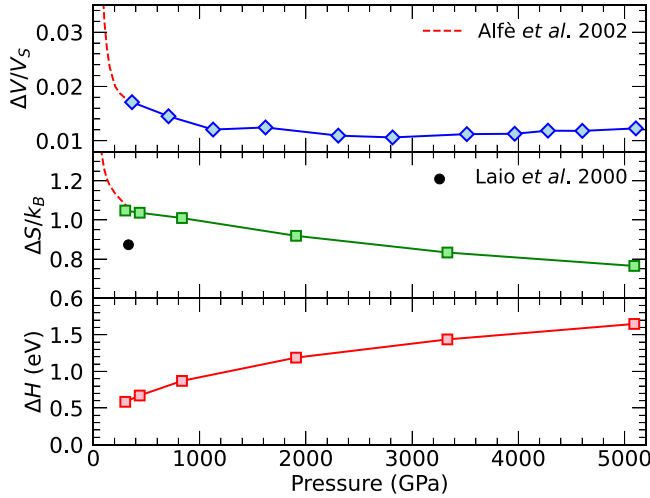$$T_m(P) = T_0 \left(1 + \frac{(P - P_0)}{a} \right)^{1/c} \quad (9)$$

FIG. 6. Fractional change in volume, entropy, and enthalpy difference (latent heat) between liquid and solid iron along the melting line as a function of pressure. The black circle and dashed red lines show results from Refs. [73] and [20], respectively.

with the parameters $a = 434.822$ GPa and $c = 1.839$ in addition to $P_0 = 300$ GPa and $T_0 = 6469$ K.

The fractional changes of volumes, entropy, and latent heat of fusion (ΔV, ΔS, and ΔH, respectively) along the melting line are shown in Fig. 6 as a function of pressure. At 300 GPa, the volume increase upon melting is 0.116 Å^3 per atom, which correspond to a fractional decrease in density of 1.6%. The enthalpy and entropy of melting, respectively, are 1.06×10^6 J/kg (0.61 eV/atom) and 1.05 k_B/atom at this pressure. These results are an agreement with previous findings at similar conditions [20,73,74]. Our entropies of melting, however, decrease with pressure and are slightly higher than the those reported by Kraus *et al.* [24], who assumed a constant entropy of melting of $\Delta S = 0.77$ k_B to derive the melting temperatures between 300 and 1000 GPa. We determined that this value decreased from 1.05 to 0.8 k_B/atom over this pressure interval. Novel techniques based on latent heat to detect melting may confirm these values in the near future [75].

As pressure increases, the volume difference between the solid and the liquid decreases and becomes as small as 0.038 Å^3 at 5000 GPa, which still represents a fractional difference of 1.21%. Despite this decrease, we always find the solid to be denser than the liquid at the same pressure and temperature, which implies a positive slope for the melting curve. We used these values to calculate the slopes of the melting line from the Clausius-Clapeyron equation $dT_m/dP = \Delta V/\Delta S$. The slopes decrease from 8.6 K/GPa at 300 GPa to 2.6 K/GPa at 5000 GPa, and are consistent with slope of the fitted melting curve in Eq. (9).

In order to study the crystallization of planetary cores, we calculated adiabats of solid and liquid iron. We obtained the Gibbs free energy for both phases along five different isotherms, for pressures ranging from 500 to 5000 GPa. The entropies were then obtained from the free energies as $S = (E - F)/T$, and a spline interpolation was applied to obtain the points of constant entropy. The results are shown in Fig. 7. We observe that the $S = 14$ k_B adiabat intersects the melting
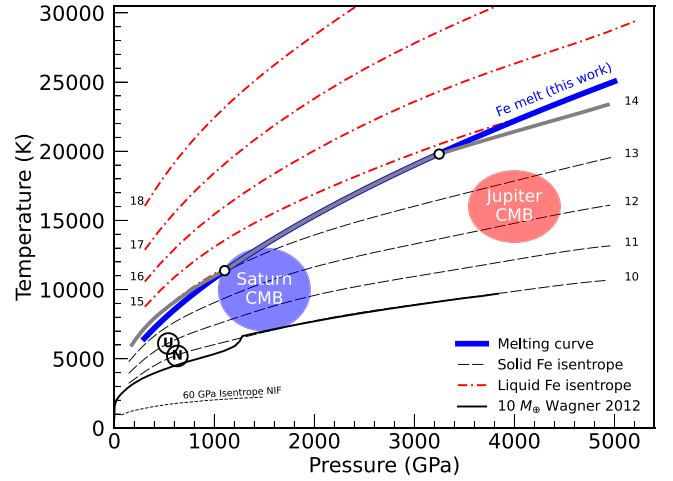

FIG. 7. Melting curve and adiabats of solid (dashed black) and liquid (dot-dashed red) iron, where the numbers indicate the respective entropy in k_B/atom. The $S = 14$ k_B/atom adiabat is shown in thick, grey line and the open circles indicate the intersection of this adiabat with the melting line. The blue line is our fit our melting points according to Eq. (9). We also show the core-mantle boundary conditions (CMB) for Uranus (U), Neptune (N), Saturn (blue area), and Jupiter (red area) [9,76] for comparison. The temperature profile of a 10 Earth mass Super-Earth model from Ref. [8] is shown in solid, black line. The 60 GPa isentrope from the ramp-compression experiments on iron from Ref. [77] is shown in short dashed line.

line at 1032 GPa and only reemerges in the solid phase at a much higher pressure 3247 GPa. This implies there exists an extended solid-liquid coexistence region along the adiabat, which has implications for shock and ramp compression experiments that are designed to measure the melting temperature by compressing liquid iron. If ramp waves are employed to avoid shock heating, one can expect such experiments to be nearly adiabatic [24,77,78], such as the recent experiments performed by Kraus *et al.* [24]. Our example illustrate that up 3247 GPa, such shock experiments would generate a solid-liquid mixtures on the melting line. X-ray diffraction signal would grow with pressure as the solid fraction increases until complete solidification is obtained. This is consistent with the recent measurements by Kraus *et al.* [24] who observed a solid-liquid mixture when they started the ramp compression from approximately 580 GPa and 8500 K.

IV. RELEVANCE TO THE INTERIOR OF SUPER-EARTHS

Since our melting line is considerably higher than previous predictions, our paper will revise some of the assumptions that so far have been made about the temperature distribution in the interiors of Super-Earths. We will now discuss how existing models may have to be adjusted. For planets with 2 Earth masses or more, Gaidos *et al.* [79] predicted their iron cores to crystallize from the top and suggested iron "snow" near the core-mantle boundary (CMB), which would inhibit convection in their cores. This would shut down the magnetic dynamo and reduce their chances for harboring life [80]. Conversely, our *ab initio* simulations predict the melting line to be steeper than the adiabats up to a pressure of at least 50 Mbar.

TABLE I. Parameters for super-Earths of 2 or 5 Earth masses with terrestrial iron mass fraction of 32.5%. For each mass, we constructed two models: the coldest but still completely liquid core and the hottest but still completely frozen cores.

M M_E	Core state	P_{central} (GPa)	P_{CMB} (GPa)	T_{center} (K)	$\langle T_{\text{core}} \rangle$ (K)	T_{CMB} (K)
2.0	frozen	765	272	8931	7409	6198
2.0	liquid	768	273	9602	8069	6822
5.0	frozen	1923	672	12442	10642	8983
5.0	liquid	1997	678	15333	12457	10236

This means in Super-Earths with up 10.4 Earth masses, the core crystallization will start from the center, like on Earth. We derived this mass estimate by assuming a terrestrial iron fraction of 32.5% and by building interior models following by Seager *et al.* [5] as well as by Wilson and Militzer [10].

In the following discussion about interior temperature distributions, we will focus on terrestrial planets with up to 1.6 Earth radii and 5.8 Earth masses because observations combined mass-radius models have shown that larger planets must have a low-density outer envelope that is presumably composed of gas or ice [12]. To compare with earlier work, we construct models for planets with 2.0 and 5.0 Earth masses. Papuc and Davies [81] reported the average core temperature over an assumed lifespan of 10 billion years. According to their thermal evolution models, average core temperature of a 5.0 (2.0) Earth mass planet would start from 5100 (4300) K and then drop to 4300 (3300) K over a period of 10 Gyr. To compare with these predictions, we constructed a number of interior models based on our computed adiabats for liquid and solid iron and provide some results in Table I. Our calculations predict that the core crystallization of a 5.0 (2.0) Earth mass planet would start when average core temperature reaches 12457 (8069) K. The core crystallization would be complete when average temperature reaches 10 642 (8069) K. This means our melting calculations imply that the cores of Super-Earths with 2.0–5.0 Earth masses would be frozen for their entire 10 Gyr lifespan, if we assume the temperatures predicted by Papuc and Davies are correct. While solid cores are still assumed to cool convectively, there would be no or only a very weak dynamo, as convection in a solid body would produce such small flow speeds that would render the magnetic Reynolds number negligibly small, thus leading to the field decay by magnetic diffusion [82]. While we have performed all calculations for pure iron and light elements are known to be present in Earth core, it is reasonable to assume that they would lower the core melting temperature of Super-Earths, but this effect is unlikely to bridge the deviations between our melting predictions and the models by Papuc and Davies that approximately amount to a factor of 2 in temperature.

Noack and Breuer [83] also put together models for the interiors of Super-Earth. For planets with five Earth masses, they predict a temperature at the core-mantle boundary (CMB) of 5100 K. According to our calculations, the core crystallization of such planet would set in when the temperature at the CMB reaches 10 236 K and already be complete when it reached 8983 K.

Other authors have constructed Super-Earth models with somewhat hotter interiors. Tachinami *et al.* [84] used mixing length theory to study the thermal evolution of Super-Earth interiors. The temperature profile of five Earth mass planet did hardly change over the 10 Gyr lifespan. Respectively, 11 300 and 7540 K were predicted for the temperatures in the planet's center and at the CMB. According to our models, core crystallization would start when temperature in the planet's center 15 333 K and be already complete when it reaches 12 442 K. Wagner *et al.* [8] also used mixing length theory, and predicted that a five-Earth masses planet should have a central pressure and temperature of 2000 GPa and 8000 K, respectively. Again these assumed temperatures, imply frozen cores. In Fig. 7, we show the temperature profile of a 10 Earth mass Super-Earth model by the same authors.

Stamenkovic *et al.* [85] investigated the impact that different viscosity models have on the evolution of Super-Earths. They consider a wide range of initial CMB temperatures from 5100 to 13 500 K when they model planets of five Earth masses, which implies some planet models start with frozen cores, some with partially liquid and some with completely liquid cores. If a strongly pressure and temperature dependent viscosity is assumed, it takes ∼3 Gyr for the temperature at the CMB to cool from 13 500 to 9000 K. At this temperature, our melting calculations again imply that the core of such a planet would be completely frozen.

Recently, Boujibar *et al.* [16] constructed models for Super-Earth of different masses, core-mantle fractions, and a wide range of interior temperatures in order to determine which planets have partially crystallized cores. Buoyancy effects from core crystallization contribute to convection and the magnetic field generation [86]. Results are presented in terms of the temperature at the core-mantle boundary, which is related to the efficiency of retaining the gravitational energy from accretion. We agree with the assumptions and predictions by Boujibar *et al.* but they based their analysis on the melting line that Morard *et al.* [63] derived with *ab initio* simulations and the corresponding fit by Stixrude *et al.* [58]. As we illustrated in Fig. 5, our melting temperatures are similar up to a pressure of 1100 GPa but then are lower for higher pressures.

Currently, the initial temperature profile of a forming planet is not well characterized because no observations have been made. The temperature is controlled by the influx of the planetesimals and radiative energy exchange with the surrounding disk [81,87]. Many interior processes, like core-mantle differentiation and radioactive decay matter during the magma ocean phase cooling, are expected to be orders of magnitude faster than after mantle has solidified. Overall, the evolution of terrestrial planets is a complicated process, and as evidenced by the Earth-Venus paradox, it is not a unique process. This is particularly true for rocky exoplanets that have a significant amount of ice, as the presence of rock-ice mixtures can lead to nonlayered interiors [88–90]. With this paper, we aim to improve our understanding of one just element: the state of the iron core.

V. CONCLUSIONS

With DFT-MD simulations, we derived Gibbs free energy of solid and liquid iron and determined its melting curve in

TABLE II. Melting temperatures of iron obtained in this study using the PAW-14 pseudopotential.

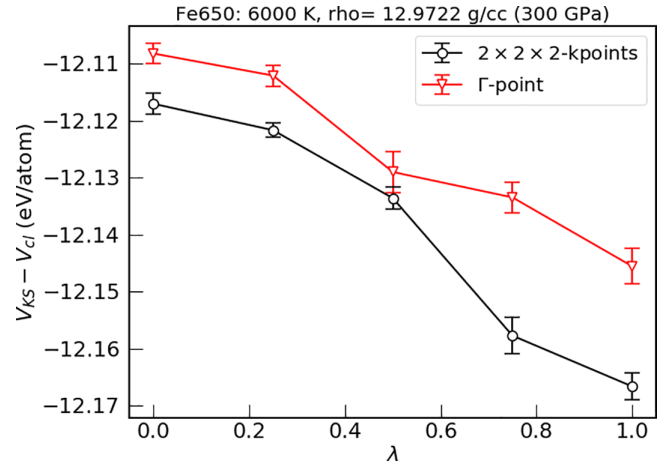| P (GPa)	T (K)
300	6468.74 ± 11.64
330	6746.95 ± 13.68
500	8023.67 ± 42.19
1000	11169.52 ± 25.75
2000	15252.75 ± 43.14
3000	18841.64 ± 36.46
4000	21784.41 ± 39.48
5000	24996.29 ± 59.80

the pressure range from 300 to 5000 GPa. We discuss the implications for ramp compression experiments and predict that they generate solid-liquid mixtures over a wide range in pressure. At 5000 GPa, we predict a melting temperature of 25 000 K, which is 5000 K higher than predicted from the extrapolation of earlier melting curves. We suggest that the initial temperature profiles in Super-Earth evolution models be investigated in more detail. For some of the published models, our melting results imply that the iron cores start out in solid form and remain frozen for the entire planet's lifetime. In this case, they would not generate a strong magnetic fields but they might still be generated in the mantles of Super-Earths [91,92]. On the other hand if the interior temperature profiles are high, the cores of Super-Earths would initially be liquid and would eventually start to crystallize from their centers. Our results also imply, if elemental iron were present in the cores of Jupiter and Saturn, it would occur in solid form (see Fig. 7). However, thermodynamic calculations [45,46] and recent models for Jupiter's interior [93,94] imply that core of giant planets have been eroded and all heavy elements have been mixed with the surrounding metallic hydrogen.

ACKNOWLEDGMENTS

FIG. 8. Convergence of the energies with respect to k-point sampling in thermodynamic integration simulations.

APPENDIX A: MELTING TEMPERATURES

The resulting melting temperatures of this study obtained from thermodynamic integration using the PAW-14 pseudopotential for iron are listed in Table II.

APPENDIX B: PSEUDOPOTENTIAL EFFECTS

Our free energy calculations using PAW-14, where the 3p inner electrons are included explicitly, give a melting temperature of 6747 K at 330 GPa, which is 688 K higher than the melting temperature we obtain at the same pressure using the PAW-8 pseudopotential. The differences in the predicted melting temperatures between PAW-14 and PAW-16 are small, but very large when compared to predictions from PAW-8 pseudopotential, which shows that the treatment of inner 3p electrons of iron at Earth core pressures and higher is extremely important, as they lead to very different predictions for the melting temperatures of iron at these conditions. We summarize these results in Table III.

APPENDIX C: CONVERGENCE WITH RESPECT TO k POINTS

We repeated a calculation at $\rho = 12.97$ g cm^{-3} (~300 GPa) and 6000 K using a $2 \times 2 \times 2$ k-point grid in our 144-atoms cells for every λ-point. As we can see in the Fig. 8, the differences in the term $\langle V_{KS} - V_{cl} \rangle$ are in general smaller than 10 meV for any given λ, which introduces a

TABLE III. Pseudopotentials effects on the melting temperature (no Frenkel correction) at 330 GPa. Our results are compared with findings by Sun *et al.* if available.

	PAW-8	PAW-14	PAW-16
T_m (K) (our paper)	6059 ± 29	6747 ± 14	6534 ± 10
T_m (K) (Sun *et al.* 2018)	5730 ± 200		6170 ± 200
ΔS_m (k_B/atom) (our paper)	1.08 ± 0.02	1.06 ± 0.02	1.06 ± 0.02
ΔS_m (k_B/atom) (Sun *et al.* 2018)	1.14 ± 0.03		1.09 ± 0.03
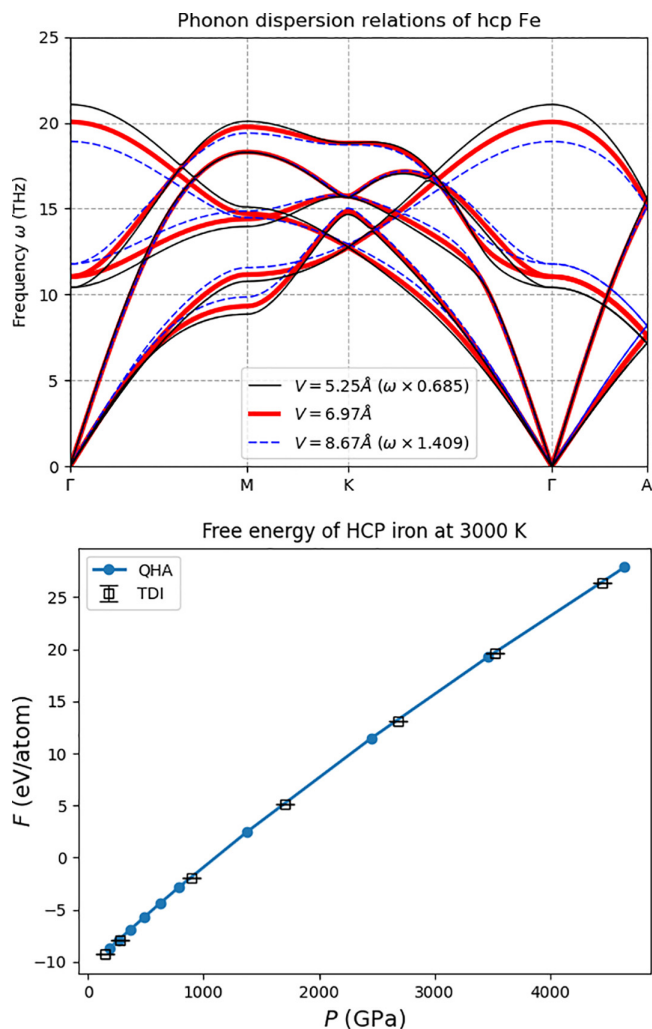
FIG. 9. Phonon-dispersion relations (top panel) of iron at three different volumes. The phonon frequencies at $6.96\,\text{Å}^3/\text{atom}$ are in remarkable agreement with those reported by Alfè [61]. The resulting free energies, obtained from QHA, are compared to those obtained from TDI in the bottom panel.

resulting error in ΔF after the thermodynamic integration that is smaller than 10 meV/atom.

APPENDIX D: PHONON CALCULATIONS

We also obtained the phonon-dispersion relations and the free energy of the hcp crystal within the quasi-harmonic approximation (QHA) to compare it with our free energies derived from thermodynamic integration. In Fig. 9, we can see that our phonon frequencies are in remarkable agreement with those derived by Alfè [61]. We also compare our Helmholtz free energies at 3000 K derived from our phonon calculations to those derived from TDI, as a function of pressure. While the trend looks consistent, the differences are much larger than 10 meV/atom, indicating the presence of anharmonic effects.
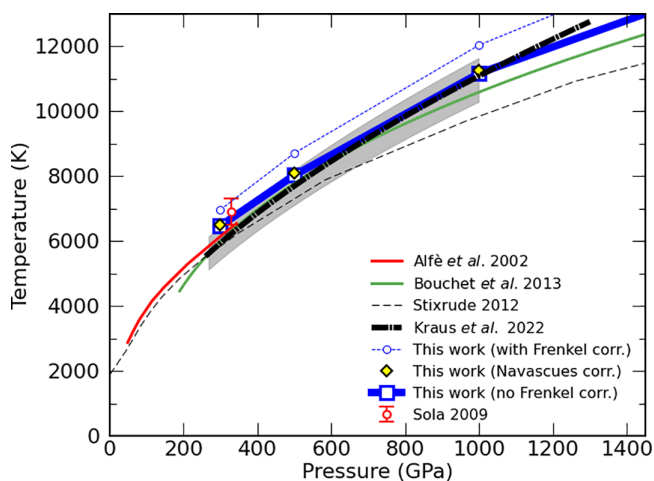
FIG. 10. Effects of the Frenkel correction of the free energy of an Einstein crystal with a fixed center of mass on the melting temperature.
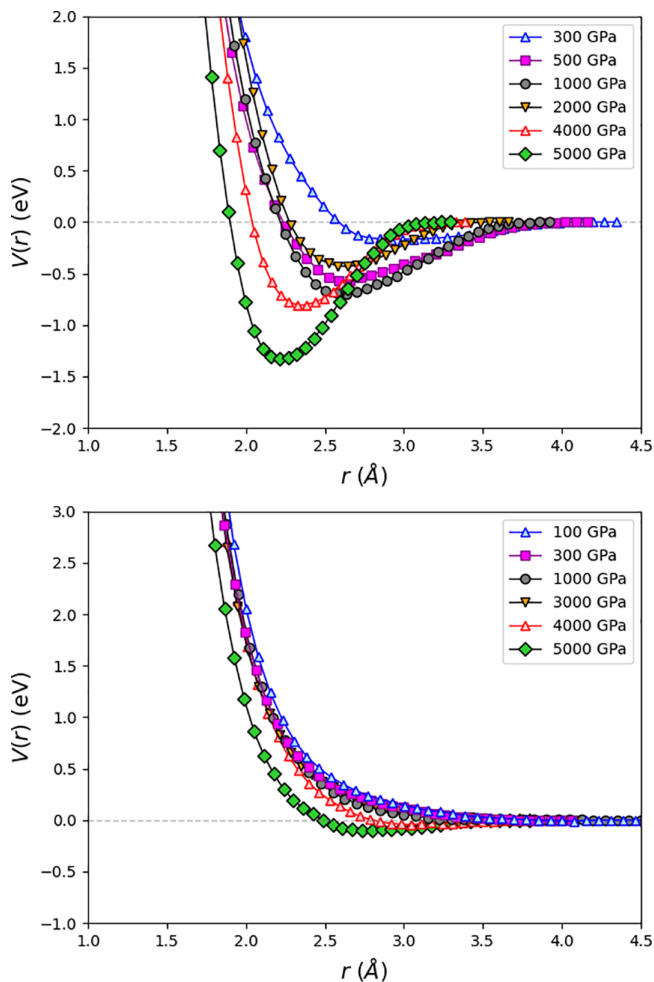
FIG. 11. Classical pair potentials for solid (top) and liquid (bottom) iron at different pressures fitted to the DFT-MD trajectories using the force matching method [49].
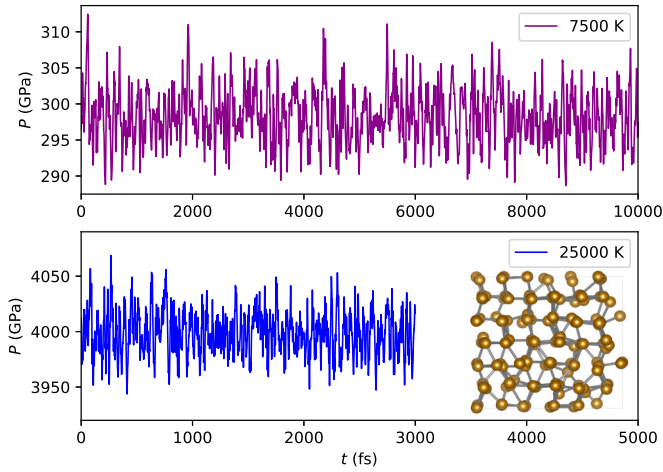
FIG. 12. Evolution of pressure as a function of time for two typical DFT-MD simulations at low (300 GPa) and high pressures (4000 GPa). Both samples are solid, as depicted by the hcp crystal in the inset. The corresponding average values of pressure are 298.243 ± 0.155 GPa and 3998.249 ± 1.071 GPa.

APPENDIX E: THE FRENKEL CORRECTION

In order to correct the free energy of the Einstein crystal to one that has a fixed center of mass, as in our DFT-MD simulations, we initially assumed the correction provided in the book by Frenkel and Ladd [51], but the recent studies of the Einstein crystal with a fixed center of mass by Navascués *et al.* [52] showed that this correction was overestimated. This leads to an artificial overstabilization of the solid and, hence, higher melting temperatures. After we applied the correction provided by Navascués *et al.*, which is so small that is effectively equivalent to applying no correction at all, our melting temperatures became lower than those where the free energy of the solid included the Frenkel correction. We can see the differences in the resulting melting temperatures of
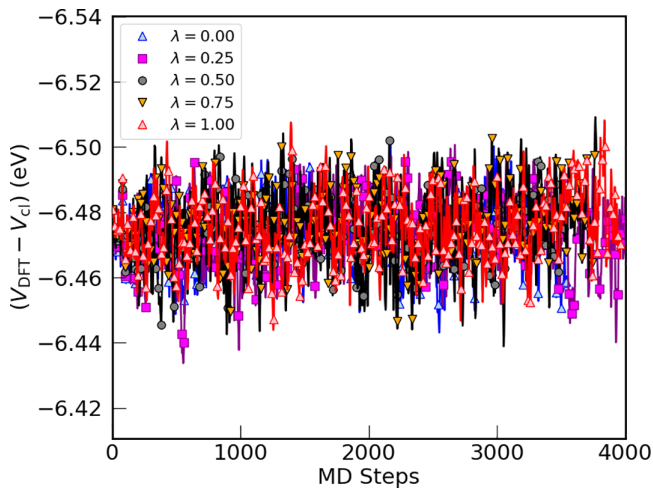
FIG. 13. Evolution of the difference $(V_{DFT} - V_{cl})$ for five values of λ during thermodynamic integration of liquid iron at 29.166 g cm^{-3} and 27 500 K. The average value for each λ has a standard errors $\sigma_{\bar{x}} = \sigma/\sqrt{n} \leqslant 2$ meV/atom.
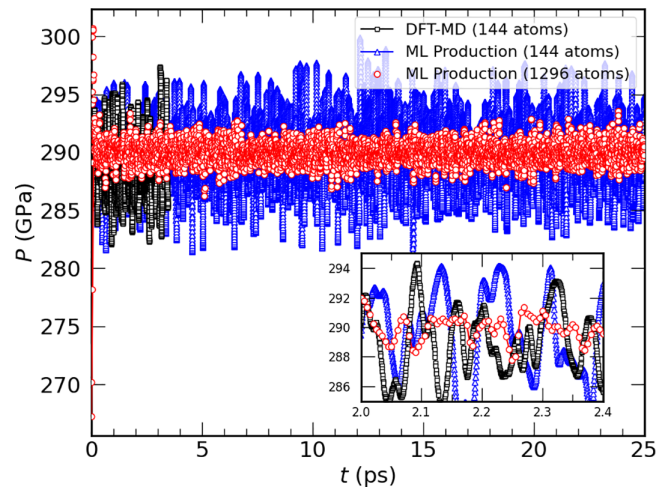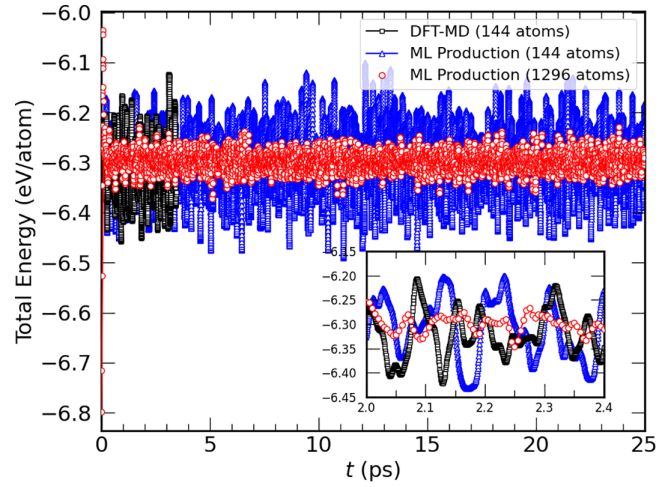
FIG. 14. Energy and pressure in molecular dynamics simulations of solid iron at 12.938 g cm^{-3} and 6000 K ($\sim$290 GPa) in the hcp phase. The DFT-MD simulations were performed using the PAW-16 pseudopotential, and the ML potential was trained on these simulations. The inset shows a zoom-in to the fluctuation in a time window of 400 fs.

APPENDIX F: CLASSICAL POTENTIALS FOR THERMODYNAMIC INTEGRATION

The intermediate systems in our thermodynamic integration procedure are governed by a classical pair potential, $V(r)$, that we construct for every density and temperature by matching the forces along the DFT-MD trajectories. For every volume V and temperature T that we choose for calculating a new value of the free energy $F(V, T)$, we fit a new classical potential using the force matching method of Izvekov and Parrinello [49]. Thus, for every single thermodynamic condition, this simple, tabulated pair potential is designed to match as close as possible the forces of the DFT-MD trajectory at those particular thermodynamic conditions. The potentials are designed to vanish for distances larger to the cutoff radius, which is set to half the length of the smallest simulation cell side. We show some of these potentials in Fig. 11.

iron after including the Frenkel and Navascués correction in Fig. 10.
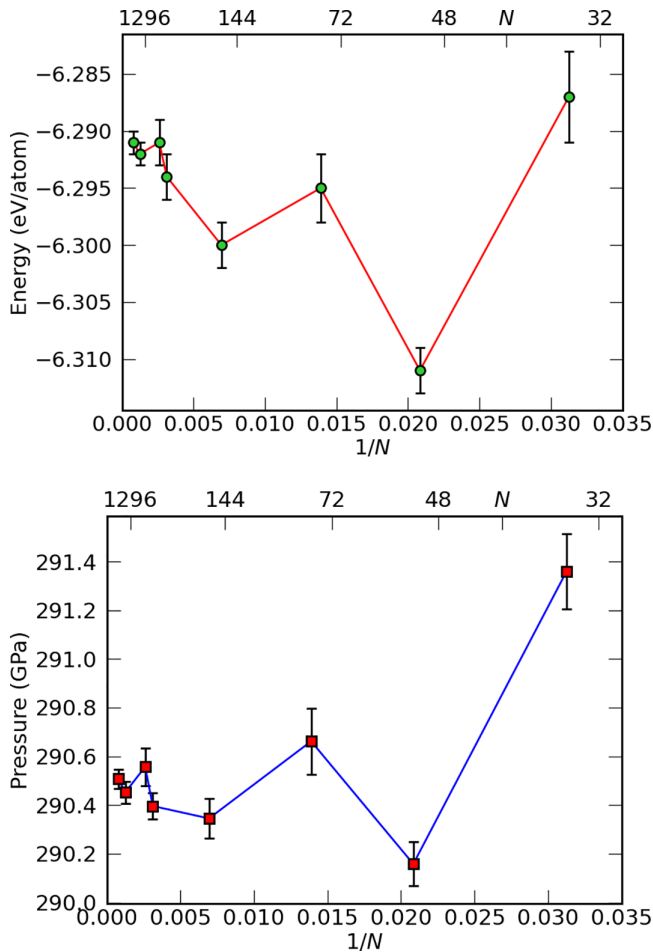
FIG. 15. Pressure and internal energy of iron derived from machine learning MD simulations at 6000 K and 12.938 g cm^{-3} using supercells with different numbers of atoms, N.

For some conditions, such as 300 GPa and 6000 K, we have repeated the thermodynamic integration procedure with a different classical potential for each phase, which was refitted to match the forces at a sightly different volume. With the new classical potentials for the solid and the liquid phases, we were able to reobtain ΔG, yielding a new value that differs from the previous one by less than 2 meV/atom, which about the size of our error bars. Thus, we demonstrate that our results are not sensitive to the classical potential used for the intermediate system.

APPENDIX G: CONVERGENCE OF THERMODYNAMIC PROPERTIES

In order to ensure the convergence of the thermodynamic quantities, such as pressure and energy, we must run each simulations long enough to allow the system to reach equilibrium, with a well defined mean value and error bars that are small enough to reach the precision we require for thermodynamic integration. In Fig. 12, we show the evolution of the pressure of the solid in two typical simulations of iron using supercells with 144 atoms. These simulations were are part of a set of simulations using thermodynamic integration using $\lambda = 1$ (forces and energies correspond to the DFT system).
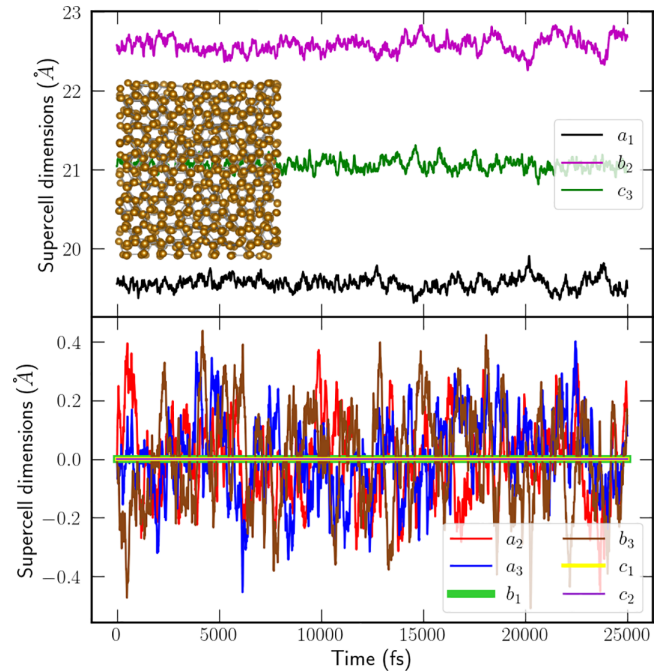
FIG. 16. Evolution of the cell dimensions of our supercell with 1296 atoms at constant pressure of $P_0 = 289.204$ GPa. The simulation cell vectors $\mathbf{a} = (a_1, a_2, a_3)$, $\mathbf{b} = (b_1, b_2, b_3)$, and $\mathbf{c} = (c_1, c_2, c_3)$ remained perpendicular, on average, and their lengths remained oscillating around the values of the NVT simulation that led to the same average pressure.

As we smoothly switch off the classical forces with increasing λ, the behavior of the energies is much more gradual and, overall, weakly dependent on λ, as we can see in Fig. 13.

APPENDIX H: MACHINE LEARNING AND CONVERGENCE WITH RESPECT TO SYSTEM SIZE

We used the capabilities of VASP 6.4 to generate on-the-fly machine learning force fields, as implemented in Refs. [95,96]. We trained the force field on a supercell of 144 iron atoms in the hcp phase using the PAW-16 pseudopotential at 12.938 g cm^{-3} and 6000 K, which resulted in a mean pressure of 289.204 ± 0.143 GPa and a Mermin free energy of -6.3124 ± 0.0036 eV/atom. The simulation was carried out at constant volume in the canonical ensemble using the Nosé-Hoover thermostat.

As we can see in Fig. 14, we can already get a well-defined average of these quantities by simulating only 3.5 ps (7000 steps with a timestep of 0.5 fs). Even 2 ps of a DFT-MD simulation are enough to get the energy converged within 1 meV/atom. After generating a force field for solid iron at 290 GPa and 6000 K using this on-the-fly machine learning training process, we were able to simulate 50 000 steps in just 12 minutes in one node of 36 cores using the same 144 atoms supercell, which corresponds to a speedup of ×2000. Then, we used the same force field to perform a simulation of iron at the same conditions but in a much larger cell, containing of 1296 atoms ($9 \times 6 \times 6$ replicas of an orthorhombic, four-atoms unit cell of hcp). In both cases, 144 and 1296 atoms, we obtained basically the same mean value of the energy from

these simulations, with a difference of less than 16 meV/atom with respect to the smaller 144-atoms simulation, demonstrating convergence with respect to time and system size. The standard deviation decreased considerably when the system size was increased, as expected.

In Fig. 15, we show how the pressure and energy of iron change as function of the number of iron atoms in the supercell N. As we can see, a size of 144 atoms is more than enough to converge the energy and pressure with respect to the system size, considering that the associated error in fitting the machine learning potential leads to energy differences about 10 meV/atom. While larger system sizes can be reached by careful supercell design [97], the convergence with respect to system size shown in Fig. 15 demonstrates that 144 is enough to obtain reliable values of pressure and energy.

In addition, we carried simulations at constant pressure in the NPT ensemble to test the stability against fluctuations in the cell volume. Fixing the pressure in our NPT simulations

to $P_0 = 289.204$ GPa in the 1296 atoms cell, which was the average pressure in our NVT simulation at 12.938 $\mathrm{g\,cm^{-3}}$, resulted in an average density of 12.924 ± 0.0019 $\mathrm{g\,cm^{-3}}$, consistent with our NVT simulations. In Fig. 16, we show the fluctuations in the simulation cell dimensions, which shows that the simulation cell remained orthorhombic on average. The lattice constants of the hcp lattice varied by less than 0.05% during the constant-pressure simulation.

APPENDIX I: EQUATION OF STATE

In Tables IV and V, we provide the tabulated values of the total energy (E) and free energy ($F = E - TS$) per iron atom, together with the pressure (P) obtained at the different densities (ρ) and temperatures (T) explored in this study. The pseudopotential used for each calculation is listed on the last column.

TABLE IV. Free energies of solid iron obtained from thermodynamic integration, including PAW-14, PAW-8, and PAW-16 calculations. No Frenkel correction included.

Sim. ID	Size	V (Å³/Fe)	ρ (g/cc)	T (K)	P (GPa)	E (Ha/Fe)	F_{DFT} (Ha/Fe)	Pseudopotential
Fe132	144Fe	3.1220	29.7035	25000	5002.0470 ± 1.2800	$1.36241449 \pm 0.00053736$	$0.22674882 \pm 0.00016832$	PAW-14
Fe158	144Fe	3.3969	27.2991	24000	4004.2820 ± 1.9630	$1.10375957 \pm 0.00101313$	$-0.01069262 \pm 0.00027722$	PAW-14
Fe181	144Fe	3.4270	27.0598	27500	3998.6110 ± 1.8630	$1.14044400 \pm 0.00089354$	$-0.20447284 \pm 0.00023952$	PAW-14
Fe192	144Fe	3.7288	24.8695	18000	3000.9080 ± 0.4810	$0.77143696 \pm 0.00029430$	$-0.00576626 \pm 0.00014488$	PAW-14
Fe197	144Fe	3.7490	24.7352	20000	2998.8650 ± 1.0860	$0.79315727 \pm 0.00065187$	$-0.10782697 \pm 0.00014370$	PAW-14
Fe211	144Fe	3.4129	27.1716	26000	4000.6750 ± 1.1330	$1.12366198 \pm 0.00053203$	$-0.11916665 \pm 0.00019601$	PAW-14
Fe216	144Fe	3.7747	24.5670	22500	2999.6220 ± 1.6640	$0.82230909 \pm 0.00092247$	$-0.24003435 \pm 0.00015664$	PAW-14
Fe222	144Fe	4.2707	21.7137	15000	1999.7790 ± 0.8590	$0.45548402 \pm 0.00059509$	$-0.18243960 \pm 0.00009119$	PAW-14
Fe228	144Fe	5.2509	17.6603	10000	1002.2180 ± 0.2520	$0.09743111 \pm 0.00019527$	$-0.29959525 \pm 0.00006325$	PAW-14
Fe238	144Fe	3.4062	27.2247	25000	3998.2490 ± 1.0710	$1.11256370 \pm 0.00054860$	$-0.06493623 \pm 0.00018534$	PAW-14
Fe258	144Fe	5.3234	17.4198	12500	1000.2380 ± 0.6510	$0.12551121 \pm 0.00051435$	$-0.42066479 \pm 0.00011793$	PAW-14
Fe292	108Fe	3.1392	29.5400	27500	5002.3540 ± 1.9610	$1.38950296 \pm 0.00074986$	$0.09236150 \pm 0.00025881$	PAW-14
Fe297	180Fe	3.1388	29.5439	27500	5000.5090 ± 2.4170	$1.38682803 \pm 0.00096903$	$0.09124313 \pm 0.00018293$	PAW-14
Fe302	144Fe	3.1570	29.3740	30000	5007.0660 ± 3.3620	$1.41703321 \pm 0.00137374$	$-0.04816252 \pm 0.00029513$	PAW-14
Fe307	180Fe	3.1564	29.3791	30000	4999.5140 ± 3.1610	$1.41365554 \pm 0.00125622$	$-0.04903847 \pm 0.00023336$	PAW-14
Fe312	144Fe	4.3467	21.3343	20000	1998.1110 ± 1.3740	$0.51421616 \pm 0.00090800$	$-0.44407262 \pm 0.00022690$	PAW-14
Fe317	144Fe	4.2043	22.0565	10000	2000.8180 ± 0.3240	$0.40091463 \pm 0.00020407$	$0.04437866 \pm 0.00004676$	PAW-14
Fe326	144Fe	3.1288	29.6384	26000	5005.1770 ± 3.3600	$1.37435667 \pm 0.00139792$	$0.17264269 \pm 0.00021850$	PAW-14
Fe326b	144Fe	3.1288	29.6384	26000	5001.7210 ± 2.2630	$1.37284909 \pm 0.00094515$	$0.17264269 \pm 0.00021850$	PAW-14
Fe336	144Fe	4.3121	21.5050	18000	2002.3420 ± 0.9590	$0.49108057 \pm 0.00069255$	$-0.33514170 \pm 0.00027937$	PAW-14
Fe352	144Fe	3.1391	29.5411	27500	5000.5930 ± 1.2290	$1.38805776 \pm 0.00051781$	$0.09045971 \pm 0.00021674$	PAW-14
Fe352b	144Fe	3.1391	29.5411	27500	4599.8520 ± 1.9010	$1.31409420 \pm 0.00114013$	$-0.01177143 \pm 0.00045358$	PAW-16
Fe382	144Fe	6.4844	14.3009	10000	499.5060 ± 0.5180	$-0.06089824 \pm 0.00041825$	$-0.50226257 \pm 0.00008988$	PAW-14
Fe392	144Fe	6.3598	14.5810	7500	496.0940 ± 0.3710	$-0.09161250 \pm 0.00030201$	$-0.38322890 \pm 0.00005614$	PAW-14
Fe402	144Fe	5.2509	17.6603	5000	926.2860 ± 0.3630	$0.02205019 \pm 0.00025909$	$-0.12522222 \pm 0.00005397$	PAW-14
Fe407	144Fe	5.2509	17.6603	10000	1001.3900 ± 0.8850	$0.09673063 \pm 0.00063141$	$-0.29922919 \pm 0.00005513$	PAW-14
Fe412	144Fe	4.3467	21.3343	5000	1729.6300 ± 0.3300	$0.27295287 \pm 0.00020617$	$0.14058670 \pm 0.00001633$	PAW-14
Fe417	144Fe	4.3467	21.3343	10000	1809.5270 ± 0.2650	$0.34402896 \pm 0.00020900$	$-0.01757263 \pm 0.00005306$	PAW-14
Fe422	144Fe	4.3467	21.3343	15000	1899.7030 ± 0.9140	$0.42609068 \pm 0.00068361$	$-0.21664794 \pm 0.00011602$	PAW-14
Fe427	144Fe	3.7490	24.7352	5000	2712.9960 ± 0.1400	$0.56126400 \pm 0.00008166$	$0.43901659 \pm 0.00003294$	PAW-14
Fe432	144Fe	3.7490	24.7352	10000	2797.8540 ± 0.1780	$0.62949501 \pm 0.00010542$	$0.29264426 \pm 0.00004862$	PAW-14
Fe437	144Fe	3.7490	24.7352	15000	2894.5630 ± 0.7400	$0.70877573 \pm 0.00046598$	$0.10525315 \pm 0.00013912$	PAW-14
Fe442	144Fe	3.7490	24.7352	20000	2998.6800 ± 0.6260	$0.79301115 \pm 0.00040425$	$-0.10723980 \pm 0.00017022$	PAW-14
Fe447	144Fe	3.7490	24.7352	25000	3110.5910 ± 1.2710	$0.88091386 \pm 0.00075225$	$-0.34233930 \pm 0.00019887$	PAW-14
Fe452	144Fe	3.4129	27.1716	5000	3554.7130 ± 0.3230	$0.79548147 \pm 0.00017300$	$0.67919462 \pm 0.00002016$	PAW-14
Fe457	144Fe	3.4129	27.1716	10000	3644.4760 ± 0.4350	$0.86253555 \pm 0.00024222$	$0.53851253 \pm 0.00004462$	PAW-14

TABLE IV. *(Continued.)*

Sim. ID	Size	V (Å³/Fe)	ρ (g/cc)	T (K)	P (GPa)	E (Ha/Fe)	F_{DFT} (Ha/Fe)	Pseudopotential
Fe462	144Fe	3.4129	27.1716	15000	3746.9450 ± 1.0410	0.93977031 ± 0.00060024	0.35905608 ± 0.00013588	PAW-14
Fe467	144Fe	3.4129	27.1716	20000	3857.0670 ± 2.7440	1.02171218 ± 0.00148469	0.15494616 ± 0.00015556	PAW-14
Fe472	144Fe	3.4129	27.1716	25000	3976.5440 ± 1.5960	1.10669747 ± 0.00085197	−0.07196681 ± 0.00020872	PAW-14
Fe477	144Fe	3.1391	29.5411	5000	4480.7580 ± 0.2510	1.04119815 ± 0.00012140	0.92990730 ± 0.00001813	PAW-14
Fe482	144Fe	3.1391	29.5411	10000	4575.7660 ± 0.2230	1.10618381 ± 0.00012237	0.79550764 ± 0.00005372	PAW-14
Fe487	144Fe	3.1391	29.5411	15000	4684.4490 ± 0.1900	1.18159857 ± 0.00006687	0.62363888 ± 0.00008125	PAW-14
Fe492	144Fe	3.1391	29.5411	20000	4803.3550 ± 1.2350	1.26186769 ± 0.00055901	0.42612893 ± 0.00009158	PAW-14
Fe497	144Fe	3.1391	29.5411	25000	4933.2620 ± 1.3770	1.34608126 ± 0.00058927	0.20655488 ± 0.00022616	PAW-14
Fe506	144Fe	7.3106	12.6847	7500	297.6820 ± 0.3610	−0.15282630 ± 0.00031065	−0.46805598 ± 0.00007787	PAW-14
Fe516	144Fe	7.0530	13.1481	5000	306.2070 ± 0.3960	−0.17999521 ± 0.00031351	−0.35356506 ± 0.00002606	PAW-14
Fe654	144Fe	7.1486	12.9722	6000	302.7040 ± 0.0950	−0.16968387 ± 0.00008015	−0.39701455 ± 0.00004103	PAW-14
Fe654b	144Fe	7.1486	12.9722	6000	302.1560 ± 0.5300	−0.16996346 ± 0.00042359	−0.39799846 ± 0.00005319	PAW-14
Fe1500	72Fe	7.2136	12.8553	6000	299.9850 ± 0.3770	−0.16556906 ± 0.00031260	−0.39782377 ± 0.00007332	PAW-14
Fe1554	128Fe	7.1914	12.8949	6000	302.2360 ± 0.2380	−0.16406270 ± 0.00021160	−0.39817751 ± 0.00007724	PAW-14, bcc
Fe1559	144Fe	5.2509	17.6603	15000	1088.9610 ± 1.0210	0.18409984 ± 0.00078342	−0.51665947 ± 0.00022193	PAW-14
Fe1564	144Fe	4.7562	19.4973	15000	1458.8090 ± 1.1870	0.29512118 ± 0.00088340	−0.37346472 ± 0.00017142	PAW-14
Fe1569	144Fe	8.1170	11.4246	5000	167.9520 ± 0.4510	−0.21964194 ± 0.00037517	−0.41022439 ± 0.00006894	PAW-14
Fe1574	144Fe	5.2509	17.6603	7500	962.3650 ± 0.1980	0.05757173 ± 0.00015628	−0.20606046 ± 0.00003455	PAW-14
Fe1579	144Fe	4.3467	21.3343	7500	1767.9870 ± 0.1460	0.30659877 ± 0.00010308	0.06758909 ± 0.00002409	PAW-14
Fe1584	144Fe	3.7490	24.7352	7500	2754.0380 ± 0.0750	0.59384081 ± 0.00006234	0.37153358 ± 0.00004128	PAW-14
Fe1589	144Fe	3.4129	27.1716	7500	3597.6510 ± 0.2330	0.82712261 ± 0.00013281	0.61439034 ± 0.00004447	PAW-14
Fe1594	144Fe	3.1391	29.5411	7500	4526.7070 ± 0.1680	1.07211731 ± 0.00008620	0.86819281 ± 0.00003206	PAW-14
Fe1599	144Fe	8.1170	11.4246	3000	143.3960 ± 0.2810	−0.24982281 ± 0.00022501	−0.34160172 ± 0.00007540	PAW-14
Fe1604	144Fe	7.0530	13.1481	3000	282.4770 ± 0.3400	−0.20735695 ± 0.00026905	−0.29108615 ± 0.00004376	PAW-14
Fe1609	144Fe	5.2509	17.6603	3000	900.6000 ± 0.0490	−0.00237970 ± 0.00003057	−0.07211377 ± 0.00002110	PAW-14
Fe1614	144Fe	4.3467	21.3343	3000	1701.9980 ± 0.0560	0.24945992 ± 0.00002903	0.18763142 ± 0.00002746	PAW-14
Fe1619	144Fe	3.7490	24.7352	3000	2683.5580 ± 0.0360	0.53828166 ± 0.00001686	0.48232480 ± 0.00002056	PAW-14
Fe1624	144Fe	3.4129	27.1716	3000	3525.3430 ± 0.1520	0.77321886 ± 0.00008714	0.71988427 ± 0.00003886	PAW-14
Fe1629	144Fe	3.1391	29.5411	3000	4447.4470 ± 0.0550	1.01927423 ± 0.00003464	0.96891875 ± 0.00001872	PAW-14
Fe1691	144Fe	7.1108	13.0410	6000	301.0390 ± 0.2430	−0.16248956 ± 0.00026066	−0.39379509 ± 0.00004845	PAW-8
Fe1696	144Fe	7.1023	13.0568	6000	301.1550 ± 0.1670	−0.16576437 ± 0.00016003	−0.39437747 ± 0.00005134	PAW-16
Fe1711	144Fe	7.1175	13.0288	7500	321.1710 ± 0.6700	−0.13624500 ± 0.00071198	−0.45531385 ± 0.00012403	PAW-8
Fe1716	144Fe	7.2431	12.8029	7500	301.4050 ± 0.9700	−0.14575419 ± 0.00084822	−0.46486354 ± 0.00019217	PAW-16
Fe1757	144Fe	7.2053	12.8701	7000	298.9310 ± 0.5100	−0.15073766 ± 0.00049705	−0.43999349 ± 0.00008585	PAW-8
Fe1774	144Fe	3.7288	24.8695	18000	2787.6920 ± 1.6330	0.72616662 ± 0.00105179	−0.06149729 ± 0.00018966	PAW-16
Fe1784	144Fe	3.7490	24.7352	20000	2796.1790 ± 2.1000	0.75344528 ± 0.00134326	−0.16497802 ± 0.00027758	PAW-16
Fe1828	144Fe	3.0182	30.7250	25000	4991.6250 ± 1.5260	1.38162456 ± 0.00092571	0.23701548 ± 0.00030088	PAW-16
Fe1867	144Fe	3.0105	30.8031	24000	4995.7640 ± 1.6320	1.37096405 ± 0.00102727	0.29077679 ± 0.00019947	PAW-16
Fe1877	144Fe	2.9982	30.9294	22000	4997.4480 ± 1.1160	1.34952943 ± 0.00068124	0.39382166 ± 0.00016130	PAW-16
Fe1908	144Fe	2.9982	30.9294	22000	5102.5590 ± 2.0770	1.30720018 ± 0.00086007	0.36679353 ± 0.00012131	PAW-16
Fe1918	144Fe	3.0105	30.8031	24000	5105.8930 ± 1.4560	1.32809782 ± 0.00062514	0.26580492 ± 0.00015849	PAW-16
Fe1964	144Fe	3.0437	30.4674	26000	5024.6870 ± 2.2280	1.32981573 ± 0.00098073	0.13591155 ± 0.00034626	PAW-16
Fe1974	144Fe	7.2431	12.8029	6000	278.3290 ± 0.7290	−0.21682174 ± 0.00057238	−0.44668290 ± 0.00005743	PAW-16
Fe1995	144Fe	7.1656	12.9413	6000	301.3840 ± 0.8010	−0.17060139 ± 0.00067861	−0.39911113 ± 0.00009833	PAW-14
Fe2018	144Fe	7.1656	12.9413	6000	292.7290 ± 0.6260	−0.16250620 ± 0.00060229	−0.39531888 ± 0.00010678	PAW-8
Fe2040	144Fe	7.1175	13.0288	7500	323.9620 ± 1.1510	−0.13147742 ± 0.00118934	−0.45243563 ± 0.00006543	PAW-8
Fe2066	144Fe	7.1175	13.0288	6000	299.8120 ± 0.2050	−0.16296362 ± 0.00021914	−0.39419602 ± 0.00003693	PAW-8
Fe2076	144Fe	7.2431	12.8029	7000	292.6330 ± 0.4320	−0.19941357 ± 0.00036696	−0.48657459 ± 0.00008262	PAW-16
Fe2107	144Fe	7.1048	13.0520	6000	300.7960 ± 0.0940	−0.16625995 ± 0.00010906	−0.39410815 ± 0.00003795	PAW-16
Fe2136	144Fe	7.1975	12.8840	7000	300.0730 ± 0.3860	−0.15360782 ± 0.00035618	−0.44028802 ± 0.00006881	PAW-16
Fe2182	72Fe	7.1547	12.9612	6000	303.3010 ± 0.2700	−0.16803025 ± 0.00021536	−0.39702179 ± 0.00006292	PAW-14
Fe2187	144Fe	7.1547	12.9612	6000	301.8710 ± 0.1660	−0.16980924 ± 0.00014472	−0.39721826 ± 0.00002788	PAW-14
Fe2213	72Fe	7.2583	12.7762	7000	300.4490 ± 1.2080	−0.15689469 ± 0.00096960	−0.44891337 ± 0.00034021	PAW-14
Fe2218	144Fe	7.2583	12.7762	7000	299.1820 ± 0.3440	−0.15824775 ± 0.00029151	−0.44389744 ± 0.00008045	PAW-14
Fe2273	144Fe	6.9688	13.3068	6400	330.6620 ± 0.4840	−0.14854349 ± 0.00047329	−0.39953347 ± 0.00004784	PAW-8
Fe2285	144Fe	6.9688	13.3069	5800	322.3020 ± 0.1710	−0.15898574 ± 0.00017826	−0.37623477 ± 0.00003874	PAW-8
Fe2309	144Fe	6.9579	13.3277	6400	329.9970 ± 0.2930	−0.15214403 ± 0.00027193	−0.39924485 ± 0.00004408	PAW-16
Fe2322	144Fe	6.9579	13.3277	6400	331.7660 ± 0.8560	−0.15063528 ± 0.00067257	−0.39892130 ± 0.00006174	PAW-16
Fe2346	144Fe	6.9901	13.2663	6800	329.7810 ± 0.1310	−0.14729481 ± 0.00012174	−0.41714551 ± 0.00003415	PAW-16

TABLE IV. (*Continued.*)

Sim. ID	Size	V (Å^3/Fe)	ρ (g/cc)	T (K)	P (GPa)	E (Ha/Fe)	F_{DFT} (Ha/Fe)	Pseudopotential
Fe2510	240Fe	7.1486	12.9722	6000	294.1930 ± 0.0830	−0.16743435 ± 0.00007922	−0.39660917 ± 0.00002765	PAW-16
Fe2521	144Fe	3.3975	27.2948	22500	3963.9380 ± 0.6200	1.07635597 ± 0.00030220	0.05804421 ± 0.00011865	PAW-14
Fe2531	144Fe	3.3975	27.2948	21000	3929.0480 ± 0.4200	1.05128671 ± 0.00019931	0.12540926 ± 0.00009196	PAW-14
Fe2555	144Fe	3.1288	29.6384	24000	4949.8090 ± 0.4130	1.33964555 ± 0.00018650	0.26378325 ± 0.00015575	PAW-14

TABLE V. Free energies of liquid iron obtained from thermodynamic integration, including PAW-14, PAW-8, and PAW-16 calculations.

Sim. ID	Size	V (Å^3/Fe)	ρ (g/cc)	T (K)	P (GPa)	E (Ha/Fe)	F_{DFT} (Ha/Fe)	Pseudopotential
Fe137	144Fe	3.1614	29.3332	25000	4994.5650 ± 2.7170	1.38479858 ± 0.00106238	0.17943049 ± 0.00001857	PAW-14
Fe145	144Fe	3.1938	29.0351	30000	5007.9720 ± 3.5170	1.44132592 ± 0.00141143	−0.10495769 ± 0.00001696	PAW-14
Fe153	144Fe	3.4349	26.9969	24000	3988.1780 ± 5.9030	1.12152401 ± 0.00267823	−0.05078026 ± 0.00002871	PAW-14
Fe163	144Fe	3.4416	26.9449	25000	4000.7970 ± 1.8340	1.13675779 ± 0.00081318	−0.10642470 ± 0.00001837	PAW-14
Fe169	144Fe	3.4627	26.7807	27500	4002.0410 ± 1.5090	1.16500124 ± 0.00070896	−0.25205535 ± 0.00003592	PAW-14
Fe176	144Fe	3.7681	24.6102	18000	3003.7140 ± 1.2470	0.79803740 ± 0.00069791	−0.03033306 ± 0.00001706	PAW-14
Fe187	144Fe	3.7894	24.4715	20000	2997.8620 ± 1.5440	0.81790452 ± 0.00082425	−0.13888427 ± 0.00002032	PAW-14
Fe243	144Fe	3.8126	24.3225	22500	2998.8610 ± 1.1200	0.84526326 ± 0.00062363	−0.27711739 ± 0.00002306	PAW-14
Fe248	144Fe	3.4501	26.8787	26000	4003.7820 ± 1.0790	1.14916957 ± 0.00044746	−0.16414014 ± 0.00002201	PAW-14
Fe253	144Fe	3.1795	29.1655	27500	4992.6830 ± 3.4370	1.41111355 ± 0.00140851	0.03805688 ± 0.00001880	PAW-14
Fe263	144Fe	5.4556	16.9978	15000	1002.9640 ± 0.9430	0.17261043 ± 0.00064642	−0.57582821 ± 0.00001580	PAW-14
Fe268	144Fe	4.3218	21.4568	15000	1991.9220 ± 0.9920	0.47639170 ± 0.00063315	−0.20554667 ± 0.00001182	PAW-14
Fe277	144Fe	4.3892	21.1274	20000	1995.1590 ± 1.2540	0.53272689 ± 0.00081538	−0.47654951 ± 0.00000876	PAW-14
Fe282	144Fe	5.3919	17.1984	12500	1000.1030 ± 0.6110	0.14367437 ± 0.00047424	−0.44050786 ± 0.00001165	PAW-14
Fe287	144Fe	5.3178	17.4381	10000	1001.1900 ± 0.7270	0.11524986 ± 0.00054356	−0.31198404 ± 0.00001449	PAW-14
Fe331	144Fe	3.1649	29.3007	26000	5008.0340 ± 1.5740	1.39845057 ± 0.00068356	0.12898360 ± 0.00002199	PAW-14
Fe341	144Fe	4.3577	21.2802	18000	2002.6880 ± 1.4430	0.51390640 ± 0.00090219	−0.36292281 ± 0.00001439	PAW-14
Fe387	144Fe	6.5982	14.0542	10000	495.2240 ± 0.6730	−0.04979512 ± 0.00053784	−0.52084874 ± 0.00001104	PAW-14
Fe397	144Fe	6.4943	14.2790	7500	487.9890 ± 0.5980	−0.08007985 ± 0.00042708	−0.39732172 ± 0.00001605	PAW-14
Fe511	144Fe	7.4248	12.4895	7500	301.0270 ± 0.2830	−0.14073431 ± 0.00025056	−0.47934377 ± 0.00002126	PAW-14
Fe546	144Fe	5.2509	17.6603	20000	1203.3940 ± 0.8670	0.29313533 ± 0.00057666	−0.78405026 ± 0.00001900	PAW-14
Fe551	144Fe	5.2509	17.6603	25000	1282.3370 ± 2.1000	0.37634504 ± 0.00148936	−1.06297750 ± 0.00002574	PAW-14
Fe556	144Fe	5.2509	17.6603	30000	1357.2050 ± 1.8840	0.45815764 ± 0.00132139	−1.35826514 ± 0.00004197	PAW-14
Fe561	144Fe	5.2509	17.6603	35000	1437.7080 ± 1.7860	0.54488289 ± 0.00129396	−1.66765944 ± 0.00003203	PAW-14
Fe566	144Fe	4.3467	21.3343	20000	2055.2270 ± 1.4780	0.55202040 ± 0.00091484	−0.45666389 ± 0.00002033	PAW-14
Fe571	144Fe	4.3467	21.3343	25000	2145.3340 ± 1.9330	0.63378784 ± 0.00113016	−0.71796153 ± 0.00002126	PAW-14
Fe576	144Fe	4.3467	21.3343	30000	2237.8690 ± 2.2970	0.71739046 ± 0.00129994	−0.99596488 ± 0.00002032	PAW-14
Fe581	144Fe	4.3467	21.3343	35000	2323.4660 ± 2.6250	0.79720395 ± 0.00147022	−1.28800616 ± 0.00003412	PAW-14
Fe586	144Fe	3.7490	24.7352	20000	3081.3070 ± 3.0230	0.83928305 ± 0.00157459	−0.11106951 ± 0.00002872	PAW-14
Fe591	144Fe	3.7490	24.7352	25000	3196.3900 ± 3.1010	0.92697628 ± 0.00152422	−0.35856289 ± 0.00002558	PAW-14
Fe596	144Fe	3.7490	24.7352	30000	3301.8890 ± 2.5880	1.01007444 ± 0.00141635	−0.62300188 ± 0.00004320	PAW-14
Fe601	144Fe	3.7490	24.7352	35000	3412.1420 ± 3.5960	1.09452698 ± 0.00178233	−0.90139361 ± 0.00003122	PAW-14
Fe606	144Fe	3.4129	27.1716	20000	3932.7980 ± 6.2970	1.05719951 ± 0.00304946	0.15819153 ± 0.00003120	PAW-14
Fe611	144Fe	3.4129	27.1716	25000	4093.6890 ± 3.2310	1.16120103 ± 0.00148126	−0.07947885 ± 0.00003069	PAW-14
Fe616	144Fe	3.4129	27.1716	30000	4216.4690 ± 2.9370	1.24622781 ± 0.00133193	−0.33526810 ± 0.00003069	PAW-14
Fe621	144Fe	3.4129	27.1716	35000	4330.6370 ± 3.5570	1.32679803 ± 0.00169335	−0.60519396 ± 0.00002880	PAW-14
Fe626	144Fe	3.1391	29.5411	20000	4945.7730 ± 2.8080	1.32102202 ± 0.00104327	0.43463867 ± 0.00002665	PAW-14
Fe631	144Fe	3.1391	29.5411	25000	5072.6720 ± 3.4600	1.40160252 ± 0.00132154	0.20642203 ± 0.00002505	PAW-14
Fe636	144Fe	3.1391	29.5411	30000	5217.3800 ± 4.2370	1.48893244 ± 0.00157442	−0.04076836 ± 0.00002883	PAW-14
Fe641	144Fe	3.1391	29.5411	35000	5362.7730 ± 5.5330	1.57634956 ± 0.00197599	−0.30273840 ± 0.00002940	PAW-14
Fe649	144Fe	7.2526	12.7861	6000	308.0450 ± 0.3290	−0.15596147 ± 0.00028097	−0.40257560 ± 0.00001598	PAW-14
Fe867	144Fe	9.2743	9.9989	6000	110.6070 ± 0.2530	−0.21241066 ± 0.00020615	−0.49141685 ± 0.00003883	PAW-14
Fe872	144Fe	8.0861	11.4682	6000	200.5660 ± 0.4660	−0.18866025 ± 0.00035505	−0.45033815 ± 0.00002590	PAW-14
Fe877	144Fe	7.2983	12.7060	6000	300.9020 ± 0.7610	−0.15829104 ± 0.00061190	−0.40581291 ± 0.00001712	PAW-14
Fe882	144Fe	6.9916	13.2635	6000	348.8240 ± 0.3670	−0.14530885 ± 0.00029260	−0.59584650 ± 0.00002318	PAW-14

TABLE V. *(Continued.)*

Sim. ID	Size	V (Å^3/Fe)	ρ (g/cc)	T (K)	P (GPa)	E (Ha/Fe)	F_{DFT} (Ha/Fe)	Pseudopotential
Fe887	144Fe	9.7809	9.4810	7500	100.6080 ± 0.5980	−0.19510321 ± 0.00042568	−0.57699824 ± 0.00002437	PAW-14
Fe892	144Fe	8.2653	11.2195	7500	199.7080 ± 0.4610	−0.17164311 ± 0.00037906	−0.52688551 ± 0.00001901	PAW-14
Fe897	144Fe	7.4352	12.4722	7500	296.9100 ± 0.7750	−0.14344256 ± 0.00060390	−0.48007862 ± 0.00001676	PAW-14
Fe902	144Fe	6.8621	13.5137	7500	401.3540 ± 0.7810	−0.10841761 ± 0.00063068	−0.43446457 ± 0.00001782	PAW-14
Fe907	144Fe	6.4453	14.3878	7500	500.4130 ± 0.5350	−0.07647014 ± 0.00041369	−0.39167697 ± 0.00001568	PAW-14
Fe912	144Fe	6.1186	15.1560	7500	596.7540 ± 0.7330	−0.04555322 ± 0.00058047	−0.35227894 ± 0.00001736	PAW-14
Fe917	144Fe	5.8446	15.8664	7500	699.3100 ± 0.3520	−0.01152307 ± 0.00026830	−0.31207356 ± 0.00002318	PAW-14
Fe922	144Fe	10.3115	8.9931	10000	99.9320 ± 0.2760	−0.16297881 ± 0.00020634	−0.72316237 ± 0.00002079	PAW-14
Fe927	144Fe	8.5592	10.8343	10000	201.2630 ± 0.6070	−0.14042419 ± 0.00051669	−0.66549267 ± 0.00001740	PAW-14
Fe932	144Fe	7.6485	12.1243	10000	298.2830 ± 0.6770	−0.11305211 ± 0.00059249	−0.61418828 ± 0.00001613	PAW-14
Fe937	144Fe	7.0387	13.1748	10000	398.0160 ± 0.7070	−0.08143554 ± 0.00058507	−0.56575552 ± 0.00001821	PAW-14
Fe942	144Fe	6.5776	14.0982	10000	500.8780 ± 0.5210	−0.04769901 ± 0.00037344	−0.51837729 ± 0.00001638	PAW-14
Fe947	144Fe	6.2301	14.8845	10000	599.3030 ± 1.0080	−0.01561978 ± 0.00075236	−0.47481493 ± 0.00002028	PAW-14
Fe952	144Fe	5.9460	15.5959	10000	699.2870 ± 0.6110	0.01709919 ± 0.00048242	−0.43251015 ± 0.00002443	PAW-14
Fe957	144Fe	5.7037	16.2583	10000	801.6590 ± 0.6230	0.05106139 ± 0.00044795	−0.39087926 ± 0.00001965	PAW-14
Fe962	144Fe	5.3157	17.4452	10000	989.2210 ± 1.5860	0.10638949 ± 0.00110732	−0.31164326 ± 0.00002042	PAW-14
Fe967	144Fe	10.9011	8.5067	12500	99.0520 ± 0.4050	−0.12899630 ± 0.00029286	−0.88229780 ± 0.00003628	PAW-14
Fe972	144Fe	8.9010	10.4182	12500	196.9180 ± 0.6650	−0.11133173 ± 0.00051380	−0.81736528 ± 0.00002980	PAW-14
Fe977	144Fe	7.8781	11.7710	12500	297.5090 ± 0.8760	−0.08251134 ± 0.00069266	−0.76040812 ± 0.00002270	PAW-14
Fe982	144Fe	7.1995	12.8804	12500	397.7450 ± 0.7840	−0.05289107 ± 0.00068426	−0.70680015 ± 0.00002517	PAW-14
Fe987	144Fe	6.7031	13.8344	12500	502.0520 ± 0.7090	−0.01915899 ± 0.00055923	−0.65568176 ± 0.00002108	PAW-14
Fe992	144Fe	6.3374	14.6327	12500	601.3840 ± 0.9750	0.01329944 ± 0.00077478	−0.60951041 ± 0.00001791	PAW-14
Fe997	144Fe	6.0294	15.3801	12500	706.5020 ± 0.7900	0.04850180 ± 0.00057878	−0.56346953 ± 0.00001378	PAW-14
Fe1002	144Fe	5.7694	16.0732	12500	810.5450 ± 0.9520	0.08215410 ± 0.00069380	−0.51837126 ± 0.00001729	PAW-14
Fe1007	144Fe	11.5261	8.0455	15000	97.7030 ± 0.3870	−0.09387886 ± 0.00033007	−1.05192122 ± 0.00002258	PAW-14
Fe1012	144Fe	6.8603	13.5174	15000	498.0860 ± 0.7770	0.00955313 ± 0.00061628	−0.80555141 ± 0.00001642	PAW-14
Fe1017	144Fe	5.8791	15.7733	15000	798.6650 ± 0.9780	0.10605700 ± 0.00067551	−0.66287041 ± 0.00001969	PAW-14
Fe1022	144Fe	5.4598	16.9848	15000	1000.4780 ± 1.0290	0.17159009 ± 0.00068289	−0.57683003 ± 0.00001435	PAW-14
Fe1027	144Fe	5.1370	18.0519	15000	1198.6120 ± 1.0060	0.23363252 ± 0.00073686	−0.49565547 ± 0.00001297	PAW-14
Fe1032	144Fe	4.8742	19.0252	15000	1404.7700 ± 1.0330	0.29979882 ± 0.00069222	−0.41734259 ± 0.00001258	PAW-14
Fe1037	144Fe	4.7638	19.4663	15000	1500.9290 ± 1.2860	0.32866491 ± 0.00086047	−0.38060305 ± 0.00001371	PAW-14
Fe1042	144Fe	3.7689	24.6046	15000	2915.4580 ± 4.3900	0.73354280 ± 0.00252823	0.09950743 ± 0.00002282	PAW-14
Fe1047	144Fe	12.1392	7.6391	18000	102.2910 ± 0.5290	−0.04965161 ± 0.00040023	−1.26321950 ± 0.00002649	PAW-14
Fe1052	144Fe	7.0330	13.1854	18000	495.7880 ± 1.1860	0.04435750 ± 0.00092524	−0.99339361 ± 0.00002133	PAW-14
Fe1057	144Fe	5.5496	16.7098	18000	996.5420 ± 1.3920	0.20418588 ± 0.00099772	−0.75218488 ± 0.00001185	PAW-14
Fe1062	144Fe	4.8202	19.2382	18000	1499.2890 ± 1.0540	0.36140892 ± 0.00074136	−0.54688333 ± 0.00001760	PAW-14
Fe1067	144Fe	4.3587	21.2753	18000	1997.0520 ± 1.7590	0.51070639 ± 0.00113278	−0.36315238 ± 0.00001535	PAW-14
Fe1072	144Fe	4.2141	22.0056	18000	2199.5150 ± 2.1060	0.57079408 ± 0.00133188	−0.29365967 ± 0.00001285	PAW-14
Fe1077	144Fe	4.0272	23.0264	18000	2495.4840 ± 1.1770	0.65526805 ± 0.00073232	−0.19337047 ± 0.00001457	PAW-14
Fe1082	144Fe	12.4502	7.4483	20000	106.2290 ± 0.7780	−0.02100781 ± 0.00069991	−1.40732822 ± 0.00002067	PAW-14
Fe1087	144Fe	7.1304	13.0052	20000	498.2900 ± 1.3180	0.06944099 ± 0.00097431	−1.12188554 ± 0.00001379	PAW-14
Fe1092	144Fe	5.6001	16.5590	20000	999.6020 ± 1.1830	0.22839574 ± 0.00087949	−0.87201306 ± 0.00001175	PAW-14
Fe1097	144Fe	4.8594	19.0833	20000	1499.6940 ± 0.9580	0.38469879 ± 0.00065332	−0.66334418 ± 0.00001263	PAW-14
Fe1102	144Fe	4.3858	21.1439	20000	2001.6430 ± 1.4670	0.53510860 ± 0.00090677	−0.47481361 ± 0.00001211	PAW-14
Fe1107	144Fe	4.2396	21.8728	20000	2195.0350 ± 1.9470	0.59023132 ± 0.00121534	−0.40447630 ± 0.00001747	PAW-14
Fe1112	144Fe	4.0454	22.9228	20000	2505.7610 ± 1.6210	0.68110210 ± 0.00101806	−0.29990972 ± 0.00001103	PAW-14
Fe1117	144Fe	3.7433	24.7727	20000	3092.0770 ± 1.6970	0.84168437 ± 0.00091070	−0.10674354 ± 0.00002060	PAW-14
Fe1122	144Fe	12.8592	7.2114	22500	112.2010 ± 0.7820	0.01607825 ± 0.00074141	−1.59361861 ± 0.00003311	PAW-14
Fe1127	144Fe	7.2553	12.7814	22500	503.4930 ± 0.8880	0.10305469 ± 0.00068836	−1.28806918 ± 0.00001251	PAW-14
Fe1132	144Fe	5.6752	16.3400	22500	999.3560 ± 1.4260	0.25817100 ± 0.00101661	−1.02965824 ± 0.00001640	PAW-14
Fe1137	144Fe	4.4248	20.9575	22500	2000.9210 ± 1.1840	0.56402757 ± 0.00067394	−0.62175718 ± 0.00001747	PAW-14
Fe1142	144Fe	4.0770	22.7455	22500	2500.9760 ± 2.1570	0.70709430 ± 0.00126354	−0.44330308 ± 0.00001987	PAW-14
Fe1147	144Fe	3.8129	24.3207	22500	3000.5080 ± 1.5720	0.84622135 ± 0.00086023	−0.27723308 ± 0.00001598	PAW-14
Fe1152	144Fe	3.6018	25.7466	22500	3495.1180 ± 1.7920	0.97857565 ± 0.00094681	−0.12051517 ± 0.00001560	PAW-14
Fe1157	144Fe	3.4293	27.0411	22500	3985.8590 ± 2.3070	1.10750579 ± 0.00107289	0.02710375 ± 0.00001873	PAW-14
Fe1162	144Fe	13.1975	7.0265	24000	112.2740 ± 0.7060	0.03692891 ± 0.00068499	−1.71027396 ± 0.00005099	PAW-14
Fe1167	144Fe	5.7151	16.2261	24000	1001.2130 ± 1.0790	0.27652244 ± 0.00079987	−1.12563140 ± 0.00002294	PAW-14

TABLE V. (*Continued.*)

Sim. ID	Size	V (Å³/Fe)	ρ (g/cc)	T (K)	P (GPa)	E (Ha/Fe)	F_{DFT} (Ha/Fe)	Pseudopotential
Fe1172	144Fe	4.4462	20.8564	24000	1998.6380 ± 1.6920	0.57945927 ± 0.00111339	−0.71134848 ± 0.00001524	PAW-14
Fe1177	144Fe	3.8273	24.2293	24000	3001.1320 ± 1.7710	0.86273218 ± 0.00094484	−0.36283512 ± 0.00001881	PAW-14
Fe1182	144Fe	3.6130	25.6661	24000	3500.4500 ± 1.5680	0.99653747 ± 0.00079357	−0.20371660 ± 0.00002742	PAW-14
Fe1187	144Fe	3.4348	26.9978	24000	4001.8920 ± 1.8060	1.12697040 ± 0.00087811	−0.05069922 ± 0.00001927	PAW-14
Fe1192	144Fe	3.2831	28.2451	24000	4507.1210 ± 1.9380	1.25537372 ± 0.00083926	0.09724833 ± 0.00001481	PAW-14
Fe1197	144Fe	3.1550	29.3926	24000	4994.7340 ± 2.3990	1.37465053 ± 0.00089825	0.23626271 ± 0.00001781	PAW-14
Fe1202	144Fe	13.9386	6.6530	25000	100.2030 ± 0.6010	0.04895646 ± 0.00056361	−1.80171181 ± 0.00004037	PAW-14
Fe1207	144Fe	5.7480	16.1330	25000	1000.1930 ± 0.9850	0.28842748 ± 0.00073726	−1.19201993 ± 0.00001350	PAW-14
Fe1212	144Fe	4.4600	20.7920	25000	2002.3010 ± 1.6330	0.59273872 ± 0.00102731	−0.77182278 ± 0.00001281	PAW-14
Fe1217	144Fe	3.8377	24.1635	25000	2999.0810 ± 1.4840	0.87272175 ± 0.00082447	−0.42148465 ± 0.00001306	PAW-14
Fe1222	144Fe	3.6196	25.6196	25000	3502.9100 ± 2.1680	1.00748325 ± 0.00114810	−0.25932146 ± 0.00001553	PAW-14
Fe1227	144Fe	3.4433	26.9311	25000	3986.9290 ± 2.0520	1.13123659 ± 0.00099514	−0.10807006 ± 0.00001846	PAW-14
Fe1232	144Fe	3.2935	28.1562	25000	4493.5490 ± 2.1550	1.26197214 ± 0.00085018	0.03723897 ± 0.00001524	PAW-14
Fe1237	144Fe	14.2321	6.5158	26000	100.4670 ± 0.5160	0.06336277 ± 0.00049456	−1.88318264 ± 0.00002015	PAW-14
Fe1242	144Fe	5.7797	16.0445	26000	998.3670 ± 0.8300	0.29967693 ± 0.00060268	−1.25888542 ± 0.00001812	PAW-14
Fe1247	144Fe	4.4730	20.7315	26000	2003.1390 ± 1.4880	0.60385638 ± 0.00089237	−0.83270405 ± 0.00001567	PAW-14
Fe1252	144Fe	3.8484	24.0965	26000	2995.1740 ± 1.4030	0.88227495 ± 0.00077699	−0.48107979 ± 0.00001978	PAW-14
Fe1257	144Fe	3.6299	25.5472	26000	3493.7270 ± 2.0890	1.01479485 ± 0.00107837	−0.31850358 ± 0.00001703	PAW-14
Fe1262	144Fe	3.4505	26.8749	26000	4001.1740 ± 2.5860	1.14808601 ± 0.00120571	−0.16473290 ± 0.00002240	PAW-14
Fe1267	144Fe	3.2995	28.1053	26000	4493.1060 ± 2.3820	1.27151573 ± 0.00101249	−0.01743444 ± 0.00001787	PAW-14
Fe1272	144Fe	3.1641	29.3073	26000	5014.4590 ± 1.9940	1.40065227 ± 0.00073584	0.12940059 ± 0.00002647	PAW-14
Fe1277	144Fe	14.4938	6.3981	27500	102.7820 ± 0.8650	0.08450022 ± 0.00086251	−2.00236847 ± 0.00003227	PAW-14
Fe1282	144Fe	5.8239	15.9227	27500	1000.4200 ± 1.9550	0.31917914 ± 0.00149408	−1.35973833 ± 0.00001591	PAW-14
Fe1287	144Fe	4.4962	20.6247	27500	2001.0960 ± 1.6160	0.62026382 ± 0.00100317	−0.92695312 ± 0.00001338	PAW-14
Fe1292	144Fe	3.8647	23.9951	27500	2996.5510 ± 2.0110	0.90010773 ± 0.00107174	−0.57177558 ± 0.00002098	PAW-14
Fe1297	144Fe	3.6436	25.4510	27500	3500.5900 ± 2.9330	1.03484980 ± 0.00145977	−0.40758280 ± 0.00001951	PAW-14
Fe1302	144Fe	3.4622	26.7844	27500	3999.2540 ± 2.6830	1.16314781 ± 0.00119496	−0.25177356 ± 0.00002629	PAW-14
Fe1307	144Fe	3.3095	28.0205	27500	4504.3510 ± 2.9760	1.29181480 ± 0.00130799	−0.10326406 ± 0.00002068	PAW-14
Fe1312	144Fe	3.1777	29.1820	27500	4994.3330 ± 2.6980	1.41042427 ± 0.00106874	0.03999365 ± 0.00003147	PAW-14
Fe1317	144Fe	15.0352	6.1677	30000	103.5390 ± 0.7900	0.11647770 ± 0.00084756	−2.20694368 ± 0.00002693	PAW-14
Fe1322	144Fe	5.8984	15.7217	30000	1002.4880 ± 1.0820	0.35106620 ± 0.00084638	−1.53137188 ± 0.00001191	PAW-14
Fe1327	144Fe	4.5341	20.4523	30000	2001.2660 ± 1.7510	0.64908634 ± 0.00101871	−1.08689006 ± 0.00001715	PAW-14
Fe1332	144Fe	3.8878	23.8520	30000	3002.6660 ± 2.7090	0.92998594 ± 0.00142882	−0.72315187 ± 0.00001969	PAW-14
Fe1337	144Fe	3.6651	25.3018	30000	3498.2040 ± 2.2180	1.06033572 ± 0.00109558	−0.55765868 ± 0.00001506	PAW-14
Fe1342	144Fe	3.4817	26.6346	30000	3992.8100 ± 2.0560	1.18696596 ± 0.00085843	−0.40028514 ± 0.00001785	PAW-14
Fe1347	144Fe	3.1954	29.0208	30000	4999.7660 ± 2.7300	1.43912689 ± 0.00111562	−0.10671397 ± 0.00001753	PAW-14
Fe1352	144Fe	3.0755	30.1526	30000	5500.5670 ± 4.1750	1.55625225 ± 0.00158784	0.03767278 ± 0.00002441	PAW-14
Fe1495	72Fe	7.3281	12.6544	6000	299.8190 ± 0.4690	−0.15700300 ± 0.00039989	−0.40760628 ± 0.00001990	PAW-14
Fe1507	72Fe	7.4349	12.4727	7500	300.6500 ± 0.4570	−0.14090327 ± 0.00038482	−0.48021161 ± 0.00002017	PAW-14
Fe1534	144Fe	5.3921	17.1979	12500	999.4480 ± 1.0210	0.14288948 ± 0.00073316	−0.44044867 ± 0.00001774	PAW-14
Fe1539	144Fe	5.1165	18.1244	12500	1172.5120 ± 0.7990	0.19755914 ± 0.00055587	−0.37211371 ± 0.00002112	PAW-14
Fe1544	144Fe	4.8980	18.9329	12500	1336.3640 ± 0.7540	0.24814360 ± 0.00051671	−0.30912624 ± 0.00001645	PAW-14
Fe1549	144Fe	4.8037	19.3044	12500	1421.9480 ± 0.7990	0.27669477 ± 0.00056023	−0.27953167 ± 0.00001313	PAW-14
Fe1701	144Fe	7.2228	12.8388	6000	300.9640 ± 0.4360	−0.14996427 ± 0.00047953	−0.40202946 ± 0.00001820	PAW-8
Fe1706	144Fe	7.2285	12.8288	6000	300.9580 ± 0.4200	−0.15402131 ± 0.00031245	−0.40248728 ± 0.00002152	PAW-16
Fe1721	144Fe	7.3579	12.6032	7500	296.6390 ± 0.2770	−0.13454817 ± 0.00028220	−0.47711681 ± 0.00001536	PAW-8
Fe1726	144Fe	7.3565	12.6056	7500	300.1770 ± 0.6280	−0.13740160 ± 0.00049032	−0.47656776 ± 0.00001828	PAW-16
Fe1762	144Fe	7.2994	12.7042	7000	300.7470 ± 0.3820	−0.13847183 ± 0.00031978	−0.45052934 ± 0.00002238	PAW-8
Fe1779	144Fe	3.7681	24.6102	18000	2780.8540 ± 1.4090	0.74916681 ± 0.00087344	−0.09185207 ± 0.00007477	PAW-16
Fe1789	144Fe	3.7894	24.4715	20000	2778.4260 ± 2.2510	0.77027928 ± 0.00147026	−0.20008385 ± 0.00008027	PAW-16
Fe1833	144Fe	3.0548	30.3566	26000	4965.3940 ± 1.9080	1.41709354 ± 0.00108817	0.13687378 ± 0.00013653	PAW-16
Fe1838	144Fe	3.0539	30.3650	25000	4948.4370 ± 2.0240	1.40316566 ± 0.00116214	0.18634249 ± 0.00011257	PAW-16
Fe1872	144Fe	3.0385	30.5193	24000	4988.6890 ± 1.1750	1.40323395 ± 0.00072053	0.25260624 ± 0.00002210	PAW-16
Fe1882	144Fe	3.0315	30.5897	22000	4957.8750 ± 2.9070	1.37004188 ± 0.00168137	0.35496216 ± 0.00001667	PAW-16
Fe1913	144Fe	3.0315	30.5897	22000	5127.0950 ± 3.4680	1.34041362 ± 0.00133051	0.33628661 ± 0.00007810	PAW-16
Fe1923	144Fe	3.0385	30.5193	24000	5136.0320 ± 1.7150	1.35993043 ± 0.00062473	0.23507708 ± 0.00017890	PAW-16
Fe1969	144Fe	3.0744	30.1632	26000	5044.6020 ± 4.5200	1.35891949 ± 0.00183729	0.09861322 ± 0.00004582	PAW-16

TABLE V. (*Continued.*)

Sim. ID	Size	V (Å^3/Fe)	ρ (g/cc)	T (K)	P (GPa)	E (Ha/Fe)	F_{DFT} (Ha/Fe)	Pseudopotential
Fe1979	144Fe	7.2322	12.8222	6000	298.6240 ± 0.5590	$-0.19858725 \pm 0.00046751$	$-0.44546912 \pm 0.00003008$	PAW-16
Fe2000	144Fe	7.2978	12.7069	6000	301.0990 ± 0.3040	$-0.15968117 \pm 0.00024929$	$-0.40673097 \pm 0.00001770$	PAW-14
Fe2023	144Fe	7.2978	12.7069	6000	288.7090 ± 0.4700	$-0.15232204 \pm 0.00045275$	$-0.40480089 \pm 0.00003323$	PAW-8
Fe2045	144Fe	7.3579	12.6032	7500	297.7200 ± 0.2890	$-0.13145497 \pm 0.00028365$	$-0.47493516 \pm 0.00001862$	PAW-8
Fe2071	144Fe	7.3646	12.5917	6000	279.5640 ± 0.3850	$-0.15685761 \pm 0.00040333$	$-0.41134303 \pm 0.00001708$	PAW-8
Fe2081	144Fe	7.3704	12.5817	7000	291.6620 ± 0.5480	$-0.18879212 \pm 0.00048830$	$-0.49756670 \pm 0.00002928$	PAW-16
Fe2131	144Fe	7.2440	12.8014	6000	299.7200 ± 0.3540	$-0.15414264 \pm 0.00030562$	$-0.40293620 \pm 0.00001479$	PAW-16
Fe2141	144Fe	7.3231	12.6630	7000	299.9620 ± 0.2140	$-0.14272089 \pm 0.00017800$	$-0.45118193 \pm 0.00001626$	PAW-16
Fe2192	72Fe	7.3111	12.6839	6000	301.3090 ± 0.4120	$-0.15710184 \pm 0.00030987$	$-0.40630997 \pm 0.00002101$	PAW-14
Fe2197	144Fe	7.3111	12.6839	6000	293.1560 ± 0.3470	$-0.16327470 \pm 0.00025719$	$-0.40671380 \pm 0.00001916$	PAW-14
Fe2278	144Fe	7.0665	13.1228	6400	332.4490 ± 0.4440	$-0.13435863 \pm 0.00043563$	$-0.40753682 \pm 0.00002394$	PAW-8
Fe2290	144Fe	7.0665	13.1228	5800	323.8130 ± 0.4800	$-0.14500165 \pm 0.00045659$	$-0.38300921 \pm 0.00002735$	PAW-8
Fe2314	144Fe	7.0783	13.1011	6400	329.9800 ± 0.4830	$-0.13984677 \pm 0.00039814$	$-0.40785271 \pm 0.00002037$	PAW-16
Fe2327	144Fe	7.0783	13.1011	6400	327.5630 ± 0.6170	$-0.14211343 \pm 0.00037852$	$-0.40801792 \pm 0.00002263$	PAW-16
Fe2351	144Fe	7.1165	13.0307	6800	329.7150 ± 0.3970	$-0.13478741 \pm 0.00033083$	$-0.42770143 \pm 0.00002306$	PAW-16
Fe2516	240Fe	7.2526	12.7861	6000	298.3120 ± 0.1690	$-0.15471623 \pm 0.00014274$	$-0.40384922 \pm 0.00001060$	PAW-16
Fe2526	144Fe	3.4300	27.0355	22500	3972.0310 ± 3.9020	$1.10160091 \pm 0.00187088$	$0.02658335 \pm 0.00001801$	PAW-14
Fe2536	144Fe	3.4300	27.0355	21000	3945.9130 ± 1.3740	$1.08085845 \pm 0.00063280$	$0.09713137 \pm 0.00002119$	PAW-14
Fe2560	144Fe	3.1716	29.2381	24000	4931.4310 ± 2.8960	$1.35992420 \pm 0.00119428$	$0.21687020 \pm 0.00003299$	PAW-14

[1] W. J. Borucki, D. Koch, G. Basri, T. Brown, D. Caldwell, E. Devore, E. Dunham, T. Gautier, J. Geary, R. Gilliland *et al.*, Kepler Mission: A mission to find Earth-size planets in the habitable zone, in *Proceedings of the Conference on Towards Other Earths DARWIN/TPF and the Search for Extrasolar Terrestrial Planets, 22-25 April 2003, Heidelberg, Germany*, edited by M. Fridlund and T. Henning, (ESA Publications Division, Noordwijk, Netherlands, 2003), pp. 697–81.

[2] A. Baglin, M. Auvergne, P. Barge, J.-T. Buey, C. Catala, E. Michel, and W. Weiss, COROT Team, COROT: Asteroseismology and planet finding, in *Stellar Structure and Habitable Planet Finding*, edited by B. Battrick, F. Favata, I. W. Roxburgh, and D. Galadi, Vol. 485 (ESA Special Publication, 2002), pp. 17–24.

[3] S. R. Kane, M. L. Hill, J. F. Kasting, R. K. Kopparapu, E. V. Quintana, T. Barclay, N. M. Batalha, W. J. Borucki, D. R. Ciardi, and N. Haghighipour, A catalog of Kepler habitable zone exoplanet candidates, Astrophys. J. **830**, 1 (2016).

[4] D. Valencia, R. J. O'Connell, and D. Sasselov, Internal structure of massive terrestrial planets, Icarus **181**, 545 (2006).

[5] S. Seager, M. Kuchner, C. A. Hier-Majumder, and B. Militzer, Mass-radius relationships for solid exoplanets, Astrophys. J. **669**, 1279 (2007).

[6] D. Valencia, R. J. O'Connell, and D. D. Sasselov, The role of high-pressure experiments on determining super-Earth properties, Astrophys. Space Sci. **322**, 135 (2009).

[7] A. Léger, O. Grasset, B. Fegley, F. Codron, A. F. Albarede, P. Barge, R. Barnes, P. Cance, S. Carpy, F. Catalano *et al.*, The extreme physical properties of the CoRoT-7b super-Earth, Icarus **213**, 1 (2011).

[8] F. W. Wagner, N. Tosi, F. Sohl, H. Rauer, and T. Spohn, Rocky super-Earth interiors, Astron. Astrophys. **541**, A103 (2012).

[9] N. Nettelmann, R. Helled, J. Fortney, and R. Redmer, New indication for a dichotomy in the interior structure of Uranus and Neptune from the application of modified shape and rotation data, Planet. Space Sci. **77**, 143 (2013).

[10] H. F. Wilson and B. Militzer, Interior phase transformations and mass-radius relationships of silicon-carbon planets, Astrophys. J. **793**, 34 (2014).

[11] T. Duffy, N. Madhusudhan, and K. Lee, Mineralogy of super-Earth planets, *Treatise on Geophysics*, Vol. 2 (Elsevier, Amsterdam, 2015), pp. 149–178.

[12] L. A. Rogers, Most 1.6 earth-radius planets are not rocky, Astrophys. J. **801**, 41 (2015).

[13] H. Chen, J. C. Forbes, and A. Loeb, Habitable evaporated cores and the occurrence of panspermia near the galactic center, Astrophys. J. Lett. **855**, L1 (2017).

[14] K. Hakim, A. Rivoldini, T. Van Hoolst, S. Cottenier, J. Jaeken, T. Chust, and G. Steinle-Neumann, A new *ab initio* equation of state of hcp-Fe and its implication on the interior structure and mass-radius relations of rocky super-earths, Icarus **313**, 61 (2018).

[15] A. van den Berg, D. Yuen, K. Umemoto, M. Jacobs, and R. Wentzcovitch, Mass-dependent dynamics of terrestrial exoplanets using *ab initio* mineral properties, Icarus **317**, 412 (2019).

[16] A. Boujibar, P. Driscoll, and Y. Fei, Super-earth internal structures and initial thermal states, J. Geophys. Res.: Planets **125**, e2019JE006124 (2020).

[17] S. Tateno, K. Hirose, Y. Ohishi, and Y. Tatsumi, The structure of iron in earth's inner core, Science **330**, 359 (2010).

[18] L. Stixrude, Structure of Iron to 1 Gbar and 40000 K, Phys. Rev. Lett. **108**, 055505 (2012).

[19] A. B. Belonoshko, R. Ahuja, and B. Johansson, Quasi–*Ab Initio* Molecular Dynamic Study of Fe Melting, Phys. Rev. Lett. **84**, 3638 (2000).

[20] D. Alfè, G. D. Price, and M. J. Gillan, Iron under Earth's core conditions: Liquid-state thermodynamics and high-pressure melting curve from *ab initio* calculations, Phys. Rev. B **65**, 165118 (2002).

[21] D. Alfè, Temperature of the inner-core boundary of the Earth: Melting of iron at high pressure from first-principles coexistence simulations, Phys. Rev. B **79**, 060101(R) (2009).

[22] J. Bouchet, S. Mazevet, G. Morard, F. Guyot, and R. Musella, *Ab initio* equation of state of iron up to 1500 GPa, Phys. Rev. B **87**, 094102 (2013).

[23] R. Sinmyo, K. Hirose, and Y. Ohishi, Melting curve of iron to 290 Gpa determined in a resistance-heated diamond-anvil cell, Earth Planet. Sci. Lett. **510**, 45 (2019).

[24] R. G. Kraus, R. J. Hemley, S. J. Ali, J. L. Belof, L. X. Benedict, J. Bernier, D. Braun, R. E. Cohen, G. W. Collins, F. Coppari *et al.*, Measuring the melting curve of iron at super-earth core conditions, Science **375**, 202 (2022).

[25] J. Li, Q. Wu, J. Li, T. Xue, Y. Tan, X. Zhou, Y. Zhang, Z. Xiong, Z. Gao, and T. Sekine, Shock melting curve of iron: A consensus on the temperature at the earth's inner core boundary, Geophys. Res. Lett. **47**, e2020GL087758 (2020).

[26] E. Sola and D. Alfè, Melting of Iron under Earth's Core Conditions from Diffusion Monte Carlo Free Energy Calculations, Phys. Rev. Lett. **103**, 078501 (2009).

[27] A. B. Belonoshko, J. Fu, and G. Smirnov, Free energies of iron phases at high pressure and temperature: Molecular dynamics study, Phys. Rev. B **104**, 104103 (2021).

[28] D. C. Swift, R. G. Kraus, E. N. Loomis, D. G. Hicks, J. M. McNaney, and R. P. Johnson, Shock formation and the ideal shape of ramp compression waves, Phys. Rev. E **78**, 066115 (2008).

[29] F. González-Cataldo, B. K. Godwal, K. Driver, R. Jeanloz, and B. Militzer, Model of ramp compression of diamond from *ab initio* simulations, Phys. Rev. B **104**, 134104 (2021).

[30] S. Anzellini, A. Dewaele, M. Mezouar, P. Loubeyre, and G. Morard, Melting of iron at earth's inner core boundary based on fast x-ray diffraction, Science **340**, 464 (2013).

[31] A. B. Belonoshko, N. V. Skorodumova, A. Rosengren, and B. Johansson, Melting and critical superheating, Phys. Rev. B **73**, 012201 (2006).

[32] D. Alfè, C. Cazorla, and M. J. Gillan, The kinetics of homogeneous melting beyond the limit of superheating, J. Chem. Phys. **135**, 024102 (2011).

[33] A. B. Belonoshko and A. Rosengren, High-pressure melting curve of platinum from *ab initio* Z method, Phys. Rev. B **85**, 174104 (2012).

[34] S. Davis and G. Gutiérrez, Bayesian inference as a tool for analysis of first-principles calculations of complex materials: An application to the melting point of Ti_2GaN, Modell. Simul. Mater. Sci. Eng. **21**, 075001 (2013).

[35] D. Li, P. Zhang, and J. Yan, *Ab initio* molecular dynamics study of high-pressure melting of beryllium oxide., Sci. Rep. **4**, 4707 (2014).

[36] F. González-Cataldo, S. Davis, and G. Gutiérrez, Melting curve of SiO_2 at multimegabar pressures: Implications for gas giants and super-Earths, Sci. Rep. **6**, 26537 (2016).

[37] A. V. Karavaev, V. V. Dremov, and T. A. Pravishkina, Precise calculation of melting curves by molecular dynamics, Comput. Mater. Sci. **124**, 335 (2016).

[38] G. Kresse and J. Furthmüller, Efficient iterative schemes for *ab initio* total-energy calculations using a plane-wave basis set, Phys. Rev. B **54**, 11169 (1996).

[39] J. P. Perdew, K. Burke, and M. Ernzerhof, Generalized Gradient Approximation Made Simple, Phys. Rev. Lett. **77**, 3865 (1996).

[40] P. E. Blochl, Projector augmented-wave method, Phys. Rev. B **50**, 17953 (1994).

[41] S. G. Moustafa, A. J. Schultz, E. Zurek, and D. A. Kofke, Accurate and precise *ab initio* anharmonic free-energy calculations for metallic crystals: Application to hcp fe at high temperature and pressure, Phys. Rev. B **96**, 014117 (2017).

[42] H. F. Wilson and B. Militzer, Rocky Core Solubility in Jupiter and Giant Exoplanets, Phys. Rev. Lett. **108**, 111101 (2012).

[43] H. F. Wilson and B. Militzer, Solubility of water ice in metallic hydrogen: Consequences for core erosion in gas giant planets, Astrophys. J. **745**, 54 (2012).

[44] B. Militzer, Equation of state calculations of hydrogen-helium mixtures in solar and extrasolar giant planets, Phys. Rev. B **87**, 014202 (2013).

[45] S. M. Wahl, H. F. Wilson, and B. Militzer, Solubility of iron in metallic hydrogen and stability of dense cores in giant planets, Astrophys. J. **773**, 95 (2013).

[46] F. González-Cataldo, H. F. Wilson, and B. Militzer, Ab initio free energy calculations of the solubility of silica in metallic hydrogen and application to giant planet cores, Astrophys. J. **787**, 79 (2014).

[47] S. M. Wahl and B. Militzer, High-temperature miscibility of iron and rock during terrestrial planet formation, Earth Planet. Sci. Lett. **410**, 25 (2015).

[48] F. Soubiran and B. Militzer, Miscibility calculations for water and hydrogen in giant planets, Astrophys. J. **806**, 228 (2015).

[49] S. Izvekov, M. Parrinello, C. J. Burnham, and G. A. Voth, Effective force fields for condensed phase systems from *ab initio* molecular dynamics simulation: A new method for force-matching., J. Chem. Phys. **120**, 10896 (2004).

[50] J. Wu, F. González-Cataldo, and B. Militzer, High-pressure phase diagram of beryllium from *ab initio* free-energy calculations, Phys. Rev. B **104**, 014103 (2021).

[51] D. Frenkel and B. Smit, Chapter 7 - Free energy calculations, in *Understanding Molecular Simulation (Second Edition)*, edited by D. Frenkel and B. Smit (Academic Press, San Diego, 2002), pp. 167–200.

[52] G. Navascués and E. Velasco, Free-energy correction due to center-of-mass constraint in crystals, J. Chem. Phys. **132**, 134106 (2010).

[53] J. Wu, F. González-Cataldo, F. Soubiran, and B. Militzer, The phase diagrams of beryllium and magnesium oxide at megabar pressures, J. Phys.: Condens. Matter **34**, 144003 (2022).

[54] F. Soubiran and B. Militzer, PAnharmonicity and Phase Diagram of Magnesium Oxide in the Megabar Regime, Phys. Rev. Lett. **125**, 175701 (2020).

[55] T. Sun, J. P. Brodholt, Y. Li, and L. Vočadlo, Melting properties from *ab initio* free energy calculations: Iron at the earth's inner-core boundary, Phys. Rev. B **98**, 224301 (2018).

[56] A. Mirzaeinia, F. Feyzi, and S. M. Hashemianzadeh, Equation of state and Helmholtz free energy for the atomic system of the repulsive Lennard-Jones particles, J. Chem. Phys. **147**, 214503 (2017).

[57] Y. Sun, M. I. Mendelev, F. Zhang, X. Liu, B. Da, C.-Z. Wang, R. M. Wentzcovitch, and K.-M. Ho, *Ab initio* melting temperatures of bcc and hcp iron under the earth's inner core condition, Geophys. Res. Lett. **50**, e2022GL102447 (2023).

[58] L. Stixrude, Melting in super-earths, Philos. Trans. R. Soc. London, Ser. A **372**, 20130076 (2014).

[59] C. J. Wu, L. X. Benedict, P. C. Myint, S. Hamel, C. J. Prisbrey, and J. R. Leek, Wide-ranged multiphase equation of state for iron and model variations addressing uncertainties in high-pressure melting, Phys. Rev. B **108**, 014102 (2023).

[60] G. Morard, S. Boccato, A. D. Rosa, S. Anzellini, F. Miozzi, L. Henry, G. Garbarino, M. Mezouar, M. Harmand, F. Guyot *et al.*, Solving controversies on the iron phase diagram under high pressure, Geophys. Res. Lett. **45**, 074 (2018).

[61] D. Alfè, G. D. Price, and M. J. Gillan, Thermodynamics of hexagonal-close-packed iron under Earth's core conditions, Phys. Rev. B **64**, 045123 (2001).

[62] C. S. Yoo, N. C. Holmes, M. Ross, D. J. Webb, and C. Pike, Shock Temperatures and Melting of Iron at Earth Core Conditions, Phys. Rev. Lett. **70**, 3931 (1993).

[63] G. Morard, J. Bouchet, D. Valencia, S. Mazevet, and F. Guyot, The melting curve of iron at extreme pressures: Implications for planetary cores, High Energy Density Phys. **7**, 141 (2011).

[64] A. B. Belonoshko, T. Lukinov, J. Fu, J. Zhao, S. Davis, and S. I. Simak, Stabilization of body-centred cubic iron under inner-core conditions, Nat. Geosci. **10**, 312 (2017).

[65] A. B. Belonoshko, S. I. Simak, W. Olovsson, and O. Y. Vekilova, Elastic properties of body-centered cubic iron in earth's inner core, Phys. Rev. B **105**, 059903 (2022).

[66] M. Ghosh, S. Zhang, L. Hu, and S. Hu, Cooperative diffusion in body-centered cubic iron in earth and super-earths' inner core conditions, J. Phys.: Condens. Matter **35**, 154002 (2023).

[67] S. J. Turneaure, S. M. Sharma, and Y. M. Gupta, Crystal Structure and Melting of Fe Shock Compressed to 273 GPa: *In Situ* X-Ray Diffraction, Phys. Rev. Lett. **125**, 215702 (2020).

[68] A. J. Schultz, S. G. Moustafa, and D. A. Kofke, No system-size anomalies in entropy of bcc iron at earth's inner-core conditions, Sci. Rep. **8**, 7295 (2018).

[69] C. Sotin, O. Grasset, and A. Mocquet, Mass–radius curve for extrasolar Earth-like planets and ocean planets, Icarus **191**, 337 (2007).

[70] S. White, B. Kettle, J. Vorberger, C. L. S. Lewis, S. H. Glenzer, E. Gamboa, B. Nagler, F. Tavella, H. J. Lee, C. D. Murphy, D. O. Gericke, and D. Riley, Time-dependent effects in melting and phase change for laser-shocked iron, Phys. Rev. Res. **2**, 033366 (2020).

[71] B. Godwal, F. González-Cataldo, A. Verma, L. Stixrude, and R. Jeanloz, Stability of iron crystal structures at 0.3–1.5 TPa, Earth Planet. Sci. Lett. **409**, 299 (2015).

[72] A. Belonoshko, J. Fu, T. Bryk, S. I. Simak, and M. Mattesini, Low viscosity of the earth's inner core, Nat. Commun. **10**, 2483 (2019).

[73] A. Laio, S. Bernard, G. L. Chiarotti, S. Scandolo, and E. Tosatti, Physics of iron at earth's core conditions, Science **287**, 1027 (2000).

[74] W. J. Zhang, Z. Y. Liu, Z. L. Liu, and L. C. Cai, Melting curves and entropy of melting of iron under Earth's core conditions, Phys. Earth Planet. Inter. **244**, 69 (2015).

[75] Z. M. Geballe, N. Holtgrewe, A. Karandikar, E. Greenberg, V. B. Prakapenka, and A. F. Goncharov, Latent heat method to detect melting and freezing of metals at megabar pressures, Phys. Rev. Mater. **5**, 033803 (2021).

[76] T. Guillot, Interiors of giant planets inside and outside the solar system, Science **286**, 72 (1999).

[77] R. F. Smith, D. E. Fratanduono, D. G. Braun, T. S. Duffy, J. K. Wicks, P. M. Celliers, S. J. Ali, A. Fernandez-Pañella, R. G. Kraus, D. C. Swift *et al.*, Equation of state of iron under core conditions of large rocky exoplanets, Nat. Astron. **2**, 452 (2018).

[78] S. C. Grant, T. Ao, C. T. Seagle, A. J. Porwitzky, J.-P. Davis, K. R. Cochrane, D. H. Dolan, J.-F. Lin, T. Ditmire, and A. C. Bernstein, Equation of state measurements on iron near the melting curve at planetary core conditions by shock and ramp compressions, J. Geophys. Res.: Solid Earth **126**, e2020JB020008 (2021).

[79] E. Gaidos, C. P. Conrad, M. Manga, and J. Hernlund, Thermodynamic limits on magnetodynamos in rocky exoplanets, Astrophys. J. **718**, 596 (2010).

[80] J. I. Zuluaga and P. A. Cuartas, The role of rotation in the evolution of dynamo-generated magnetic fields in super earths, Icarus **217**, 88 (2012).

[81] A. M. Papuc and G. F. Davies, The internal activity and thermal evolution of Earth-like planets, Icarus **195**, 447 (2008).

[82] J. Jacobs, *Geomagnetism* (Elsevier, Amsterdam, 1991).

[83] L. Noack and D. Breuer, Plate tectonics on rocky exoplanets: Influence of initial conditions and mantle rheology, Planet. Space Sci. **98**, 41 (2014).

[84] C. Tachinami, H. Senshu, and S. Ida, Thermal evolution and lifetime of intrinsic magnetic fields of super-earths in habitable zones, Astrophys. J. **726**, 70 (2011).

[85] V. Stamenković, L. Noack, D. Breuer, and T. Spohn, The influence of pressure-dependent viscosity on the thermal evolution of super-earths, Astrophys. J. **748**, 41 (2012).

[86] B. A. Buffett, The thermal state of earth's core, Science **299**, 1675 (2003).

[87] C. Mordasini, P. Mollière, K.-M. Dittkrist, S. Jin, and Y. Alibert, Global models of planet formation and evolution, Int. J. Astrobiol. **14**, 201 (2015).

[88] T. Kovačević, F. González-Cataldo, S. T. Stewart, and B. Militzer, Miscibility of rock and ice in the interiors of water worlds, Sci. Rep. **12**, 1 (2022).

[89] T. Kovačević, F. González-Cataldo, and B. Militzer, The homogeneous mixing of MgO and H_2O at extreme conditions, Contrib. Plasma Phys. e202300017 (2023).

[90] A. Vazan, R. Sari, and R. Kessel, A new perspective on the interiors of ice-rich planets: Ice–rock mixture instead of ice on top of rock, Astrophys. J. **926**, 150 (2022).

[91] F. Soubiran and B. Militzer, Electrical conductivity and magnetic dynamos in magma oceans of Super-Earths, Nat. Commun. **9**, 3883 (2018).

[92] L. Stixrude, R. Scipioni, and M. P. Desjarlais, A silicate dynamo in the early earth, Nat. Commun. **11**, 935 (2020).

[93] S. M. Wahl, W. B. Hubbard, B. Militzer, T. Guillot, Y. Miguel, N. Movshovitz, Y. Kaspi, R. Helled, D. Reese, E. Galanti *et al.*, Comparing jupiter interior structure models to juno

gravity measurements and the role of a dilute core, Geophys. Res. Lett. **44**, 4649 (2017).

[94] B. Militzer *et al.*, Juno spacecraft measurements of Jupiter's gravity imply a dilute core, Planet. Sci. J. **3**, 185 (2022).

[95] R. Jinnouchi, F. Karsai, and G. Kresse, On-the-fly machine learning force field generation: Application to melting points, Phys. Rev. B **100**, 014105 (2019).

[96] R. Jinnouchi, J. Lahnsteiner, F. Karsai, G. Kresse, and M. Bokdam, Phase Transitions of Hybrid Perovskites Simulated by Machine-Learning Force Fields Trained on the Fly with Bayesian Inference, Phys. Rev. Lett. **122**, 225701 (2019).

[97] B. Militzer, Supercell design for first-principles simulations of solids and application to diamond, silica, and superionic water, High Energy Density Phys. **21**, 8 (2016).